HERSCHEL-SPIRE FOURIER TRANSFORM SPECTROMETER OBSERVATIONS OF EXCITED CO AND [C I] IN THE ANTENNAE (NGC 4038/39): WARM AND COLD MOLECULAR GAS[*]

Maximilien R. P. Schirm[1], Christine D. Wilson[1], Tara J. Parkin[1], Julia Kamenetzky[2],
Jason Glenn[2], Naseem Rangwala[2], Luigi Spinoglio[3], Miguel Pereira-Santaella[3],
Maarten Baes[4], Michael J. Barlow[5], Dave L. Clements[6], Asantha Cooray[7], Ilse De Looze[4],
Oskar Ł. Karczewski[8], Suzanne C. Madden[9], Aurélie Rémy-Ruyer[9], and Ronin Wu[9]

[1] Department of Physics and Astronomy, McMaster University, Hamilton, ON L8S 4M1, Canada; schirmr@mcmaster.ca, wilson@physics.mcmaster.ca
[2] Center for Astrophysics and Space Astronomy, 389-UCB, University of Colorado, Boulder, CO 80303, USA
[3] Istituto di Astrofisica e Planetologia Spaziali, INAF-IAPS, Via Fosso del Cavaliere 100, I-00133 Roma, Italy
[4] Sterrenkundig Observatorium, Universiteit Gent, Krijgslaan 281 S9, B-9000 Gent, Belgium
[5] Department of Physics & Astronomy, University College London, Gower Street, London WC1E 6BT, UK
[6] Astrophysics Group, Imperial College, Blackett Laboratory, Prince Consort Road, London SW7 2AZ, UK
[7] Department of Physics & Astronomy, University of California, Irvine, CA 92697, USA
[8] Department of Physics and Astronomy, University of Sussex, Brighton BN1 9QH, UK
[9] CEA, Laboratoire AIM, Irfu/SAp, Orme des Merisiers, F-91191 Gif-sur-Yvette, France

ABSTRACT

We present *Herschel* Spectral and Photometric Imaging Receiver (SPIRE) Fourier Transform Spectrometer (FTS) observations of the Antennae (NGC 4038/39), a well-studied, nearby (22 Mpc), ongoing merger between two gas-rich spiral galaxies. The SPIRE-FTS is a low spatial (FWHM $\sim 19''$–$43''$) and spectral (~ 1.2 GHz) resolution mapping spectrometer covering a large spectral range (194–671 μm, 450–1545 GHz). We detect five CO transitions ($J = 4$–3 to $J = 8$–7), both [C I] transitions, and the [N II] 205 μm transition across the entire system, which we supplement with ground-based observations of the CO $J = 1$–0, $J = 2$–1, and $J = 3$–2 transitions and *Herschel* Photodetecting Array Camera and Spectrometer (PACS) observations of [C II] and [O I] 63 μm. Using the CO and [C I] transitions, we perform both a local thermodynamic equilibrium (LTE) analysis of [C I] and a non-LTE radiative transfer analysis of CO and [C I] using the radiative transfer code RADEX along with a Bayesian likelihood analysis. We find that there are two components to the molecular gas: a cold ($T_{\rm kin} \sim 10$–30 K) and a warm ($T_{\rm kin} \gtrsim 100$ K) component. By comparing the warm gas mass to previously observed values, we determine a CO abundance in the warm gas of $x_{\rm CO} \sim 5 \times 10^{-5}$. If the CO abundance is the same in the warm and cold gas phases, this abundance corresponds to a CO $J = 1$–0 luminosity-to-mass conversion factor of $\alpha_{\rm CO} \sim 7\ M_\odot\ {\rm pc}^{-2}\ ({\rm K\ km\ s^{-1}})^{-1}$ in the cold component, similar to the value for normal spiral galaxies. We estimate the cooling from H$_2$, [C II], CO, and [O I] 63 μm to be $\sim 0.01\ L_\odot/M_\odot$. We compare photon-dominated region models to the ratio of the flux of various CO transitions, along with the ratio of the CO flux to the far-infrared flux in NGC 4038, NGC 4039, and the overlap region. We find that the densities recovered from our non-LTE analysis are consistent with a background far-ultraviolet field of strength $G_0 \sim 1000$. Finally, we find that a combination of turbulent heating, due to the ongoing merger, and supernova and stellar winds are sufficient to heat the molecular gas.

Key words: galaxies: individual (NGC 4038, NGC 4039) – galaxies: interactions – infrared: galaxies – ISM: molecules – submillimeter: galaxies

Online-only material: color figures

1. INTRODUCTION

Luminous and ultra-luminous infrared (IR) galaxies are a well-studied class of IR bright galaxies whose excess IR emission comes from dust heated by enhanced star formation activity (Cluver et al. 2010). Their enhanced star formation rate directly correlates with a star formation efficiency ~ 4–10 times greater than in normal galaxies (Genzel et al. 2010) typically seen in the form of starbursts throughout the galaxy (Sanders & Mirabel 1996). Many luminous IR galaxies (LIRGs; $L_{\rm IR} > 10^{11}\ L_\odot$) and almost all ultra-luminous IR galaxies (ULIRGs; $L_{\rm IR} > 10^{12}\ L_\odot$) are found to be in an advanced merging state between two or more galaxies (Clements et al. 1996; Sanders & Mirabel 1996); these starbursts are likely

the result of the ongoing merger (Hibbard 1997), triggered by the redistribution of material throughout the merging galaxies (Toomre & Toomre 1972). It has been suggested that all mergers undergo a period of "super starbursts" (Joseph & Wright 1985), where $\gtrsim 10^9\ M_\odot$ of stars form in $\sim 10^8$ yr (Gehrz et al. 1983).

The Antennae (NGC 4038/39, Arp 244) is a young, nearby, ongoing merger between two gas-rich spiral galaxies, NGC 4038 and NGC 4039. At a distance of only 22 ± 3 Mpc (Schweizer et al. 2008), the Antennae may represent the nearest such merger. Its IR brightness of $L_{\rm IR} = 7.5 \times 10^{10}\ L_\odot$ (Gao et al. 2001) approaches that of a LIRG and is likely the result of merger-triggered star formation. The majority of the star formation is occurring within the two nuclei (NGC 4038, NGC 4039), along with a third region where the two disks are believed to overlap (Stanford et al. 1990), also sometimes referred to as the interaction region (e.g., Schulz et al. 2007). A fourth star-forming region of interest is located to the west of NGC 4038 and is known as the "western loop." The X-ray luminosity in the

Antennae is enhanced relative to normal spiral galaxies, with 50% of the X-ray emission originating from hot diffuse gas outside of these four regions (Read et al. 1995); however, the presence of an active galactic nucleus (AGN) has been ruled out (Brandl et al. 2009).

As a result of the star formation process, most of the star clusters in the Antennae are in the two nuclei and the overlap region, with the overlap region housing the youngest ($\lesssim$5 Myr) of these star clusters; the second youngest are found in the western loop (5–10 Myr; Whitmore & Schweizer 1995; Whitmore et al. 1999). Some of the star clusters found near the overlap region are super star clusters with masses of a few $10^6\,M_\odot$ (Whitmore et al. 2010). Comparisons of *Spitzer*, *Galaxy Evolution Explorer*, *Hubble Space Telescope*, and Two Micron All Sky Survey images by Zhang et al. (2010) showed that the star formation rate itself peaks in the overlap region and western loop, agreeing with previous results by Gao et al. (2001). The overlap region exhibits characteristics of younger, more recent star formation (Zhang et al. 2010). Far-IR (FIR) spectroscopy of the Antennae with the *Infrared Space Observatory* (*ISO*) Long Wavelength Spectrometer, together with ground-based Fabry–Perot imaging spectroscopy, has been used to constrain the age of the instantaneous starburst to $(7–8)\times10^6$ yr, producing a total stellar mass of $(2.5 \pm 1.5) \times 10^8\,M_\odot$ with a luminosity of $(7 \pm 4) \times 10^{10}\,L_\odot$ (Fischer et al. 1996).

The star-forming molecular gas in the Antennae is well studied, with observations of the molecular gas tracer CO in the $J = 1$–0 (Wilson et al. 2000, 2003; Gao et al. 2001; Zhu et al. 2003; Schulz et al. 2007), $J = 2$–1 (Zhu et al. 2003; Schulz et al. 2007; Wei et al. 2012), $J = 3$–2 (Zhu et al. 2003; Schulz et al. 2007; Ueda et al. 2012), $J = 6$–5 (Bayet et al. 2006), and $J = 7$–6 (Bayet et al. 2006) transitions. Interferometric observations of the ground state transition by Wilson et al. (2000, 2003) found $\sim$100 super-giant molecular complexes (SGMCs) scattered throughout the Antennae. The seven most massive of these SGMCs consist of the two nuclei (NGC 4038 and NGC 4039) and five others located in the overlap region. Assuming a CO-to-H_2 conversion factor of $3 \times 10^{20}\,H_2\,cm^{-2}\,(K\,km\,s^{-1})^{-1}$, the molecular gas masses of the SGMCs are on the order of $10^8\,M_\odot$. In addition, recent interferometric observations of the CO $J = 3$–2 transitions by Ueda et al. (2012) show that half of the $J = 3$–2 emission originates from the overlap region. Only 30% of the giant molecular clouds (GMCs) resolved in the $J = 3$–2 map coincide with star clusters that have been detected in the optical and near-IR, suggesting that the $J = 3$–2 emission may in fact be tracing future star-forming regions.

Single-dish observations of the CO $J = 1$–0 line by Zhu et al. (2003) suggest that, assuming the same conversion factor as Wilson et al. (2000), the total molecular gas mass of the system is $1.2 \times 10^{10}\,M_\odot$, with about $\sim$40% of the total gas mass in the overlap region ($4.5 \times 10^9\,M_\odot$). Large(-scale) velocity gradient (LVG) models by Zhu et al. (2003) suggest that there are at least two phases to the molecular gas: a cold phase ($T_{kin} \sim 40$ K) and a warm phase ($T_{kin} \sim 100$ K). Bayet et al. (2006) performed a single-component LVG analysis of NGC 4038 and the overlap region, finding that in the overlap region the molecular gas of their single component is warm ($T_{kin} \sim 140$ K).

Launched in 2009, the *Herschel Space Observatory* (*Herschel*; Pilbratt et al. 2010) explores the largely unobserved wavelength range of 55–671 μm. The Spectral and Photometric Imaging Receiver (SPIRE; Griffin et al. 2010) spectrometer is the Fourier Transform Spectrometer (FTS; Naylor et al. 2010b),

an imaging spectrometer covering a total spectral range from 194 μm to 671 μm ($\sim$450 GHz to $\sim$1545 GHz). The SPIRE-FTS allows us to simultaneously observe all molecular and atomic transitions that lie within its spectral range. A total of 10 CO transitions, from $J = 4$–3 to $J = 13$–12, and both [C I] transitions at 492 GHz (609 μm) and 809 GHz (370 μm), lie within this spectral range, making the SPIRE-FTS ideal for studying both cold and warm molecular gas in extragalactic sources (e.g., see Panuzzo et al. 2010; van der Werf et al. 2010; Rangwala et al. 2011; Kamenetzky et al. 2012; Spinoglio et al. 2012; Meijerink et al. 2013; Pereira-Santaella et al. 2013).

We have obtained observations of the Antennae using the SPIRE-FTS as part of the guaranteed-time key project "Physical Processes in the Interstellar Medium of Very Nearby Galaxies" (PI: Christine Wilson), which we supplement with ground-based observations of the CO $J = 1$–0, $J = 2$–1, and $J = 3$–2 transitions. In Section 2, we present the observations and method used to reduce these data. In Section 3, we present a radiative transfer analysis used to constrain the physical properties of the gas. We discuss the implications in Section 4, where we investigate the possible heating mechanisms of the molecular gas, including modeling of photon-dominated regions (PDRs).

2. OBSERVATIONS

We observed both the nucleus of NGC 4038 (hereafter, NGC 4038) and the overlap region using the SPIRE-FTS in high spectral resolution (FWHM $= 0.048\,cm^{-1}$), full-sampling mode on 2010 December 12 (OD 572). The observation of NGC 4038 is centered at ($12^h01^m53^s.00$, $-18°52'01''.0$), while the observation of the overlap region is centered at ($12^h01^m54^s.90$, $-18°52'45''.0$). The observation IDs for the observations of NGC 4038 and the overlap region are 1342210860 and 1342210859, respectively, and the total integration time for each observation is 17,843 s, for a total integration time of 35,686 s ($\sim$10 hr). In addition to the SPIRE observations, we also present here ground-based CO $J = 1$–0 from the Nobeyama Radio Observatory (NRO; Zhu et al. 2003), along with CO $J = 2$–1 and $J = 3$–2 maps from the James Clerk Maxwell Telescope (JCMT). We also include observations of [C II] and [O I]63 from the *Herschel* Photodetecting Array Camera and Spectrometer (PACS) instrument.

2.1. FTS Data Reduction

We reduce the FTS data using a modified version of the standard Spectrometer Mapping user pipeline, the *Herschel* Interactive Processing Environment version 9.0, and the SPIRE calibration context version 8.1. Fulton et al. (2010) and Swinyard et al. (2010) described an older version of the data reduction pipeline and process. The standard mapping pipeline assumes that the source is extended enough to fill the beam uniformly. Interferometric observations of NGC 4038/39 show that the molecular gas is partially extended (Wilson et al. 2000) and does not fill the beam (Figure 1). To account for this, we apply a point-source correction to all of the detectors in both of our bolometric arrays in order to calibrate the flux accurately across the entire mapped region. Furthermore, by applying this point-source correction, we obtain a cube with the same calibration scale as our ground-based observations. This point-source correction is calculated from models and observations of Uranus and is the product of the beam area and the point source
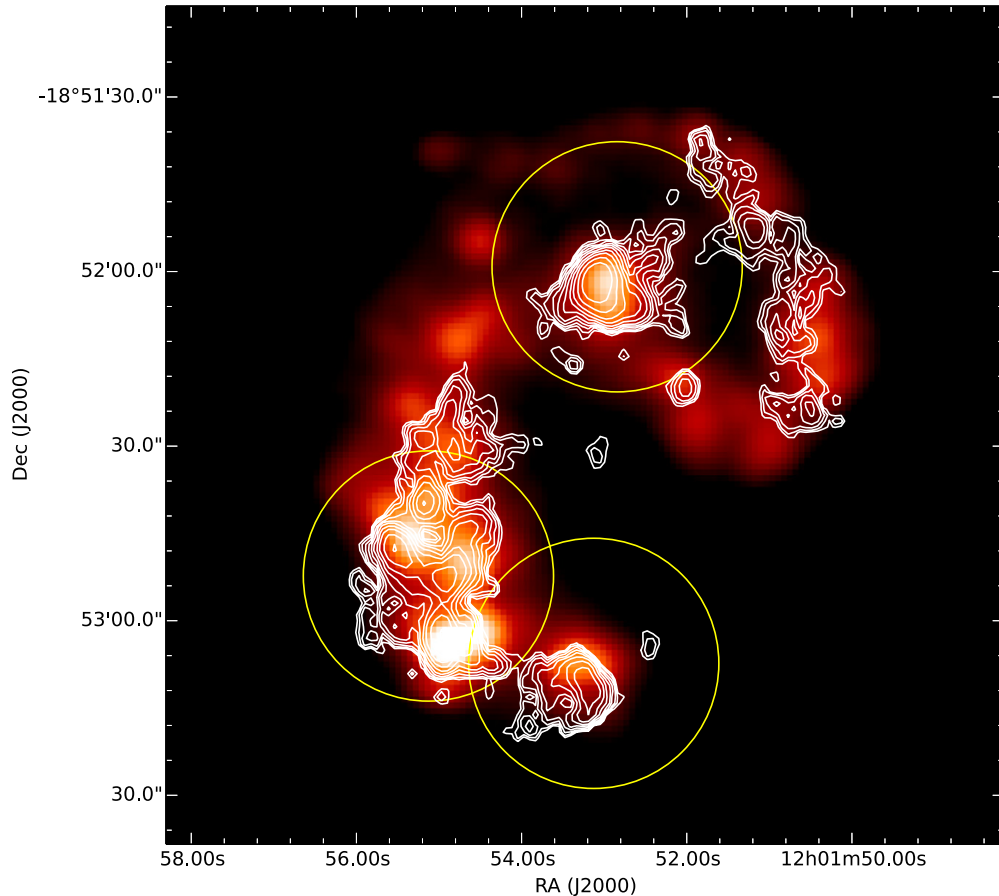
Figure 1. CO $J = 1$–0 contours from Wilson et al. (2003) overlaid on the PACS 70 μm observations of the Antennae from Klaas et al. (2010). The white contours correspond to 1%, 1.6%, 2.5%, 4%, 6%, 9.5%, 15%, 23%, 37%, and 57% of the peak intensity. The yellow circles indicate the approximate region observed for NGC 4038 (northwest), the overlap region (southeast), and NGC 4039 (southwest) for the FTS beam at $\sim$460 GHz ($\sim$43$''$).

(A color version of this figure is available in the online journal.)

coupling efficiency (see Chapter 5 of the SPIRE Observers' Manual version 2.4[10]). The correction itself varies with frequency and is unique for each individual detector.

After applying the point-source correction, we combine the observations using the *spireProjection* task into two data cubes: one for the spectrometer long wave (SLW) bolometric array and the other for the spectrometer short wave (SSW) bolometric arrays. We use a pixel size of 15$''$ for both data cubes, which we determined empirically as a balance between a sufficient number of detector hits per pixel and small pixel sizes. In addition, we create a data cube for the SSW with 3$''$ pixels for the purposes of correcting the [C II] ionized gas fraction (see Section 4.3.1). The FTS spectrum for the overlap region is shown in Figure 2.

2.1.1. Line Fitting

We detect five CO transitions in emission, from $J = 4$–3 to $J = 8$–7. We also detect the [C I] $^3P_1$–$^3P_0$ and $^3P_2$–$^3P_1$ transitions along with the [N II] ($^3P_1$–$^3P_0$) transition. We wrote a custom line fitting routine to measure the integrated intensities for all detected lines in the SLW and the SSW spectra across the entire data cube. In each pixel in the cube, the routine first removes the baseline by masking out all the lines in the spectrum and fitting a high-order polynomial to the remaining spectrum. Next, the routine fits a Sinc function to each line in the spectrum. To calculate the integrated intensity of each line,

we integrate over the entire Sinc function. In the case of the CO $J = 7$–6 and [C I] $J = 2$–1 lines, the routine fits both lines simultaneously, each with its own Sinc function. The resulting integrated intensity maps are shown in Figures 3 and 4.

2.2. Ancillary Data

2.2.1. CO J = 1–0

We obtained CO $J = 1$–0 observations of the Antennae from Zhu et al. (2003). They obtained these observations from the NRO, with a telescope beam size of 15$''$. The final map consists of three 64 point maps, each covering 68$'' \times 68''$, encompassing the CO-emitting regions in NGC 4038, the overlap region, and NGC 4039 in their entirety. We collapse the data cube using the Starlink software package (Currie et al. 2008). The total usable bandwidth was 350 MHz, corresponding to $\sim$640 km s^{-1}. The FWHM of the CO $J = 1$–0 emission line across the Antennae is $\sim$100–200 km s^{-1}; therefore, not enough bandwidth was available to estimate the uncertainty in each pixel reliably. We therefore estimate a total uncertainty, calibration included, of 20% in the final collapsed image.

2.2.2. CO J = 2–1 and CO J = 3–2

The CO $J = 2$–1 transition was observed in the Antennae using the JCMT on 2013 March 25 and 2013 April 3 as part of project M13AC09 (PI: Maximilien Schirm). These data were obtained using Receiver A3 in raster mapping mode.
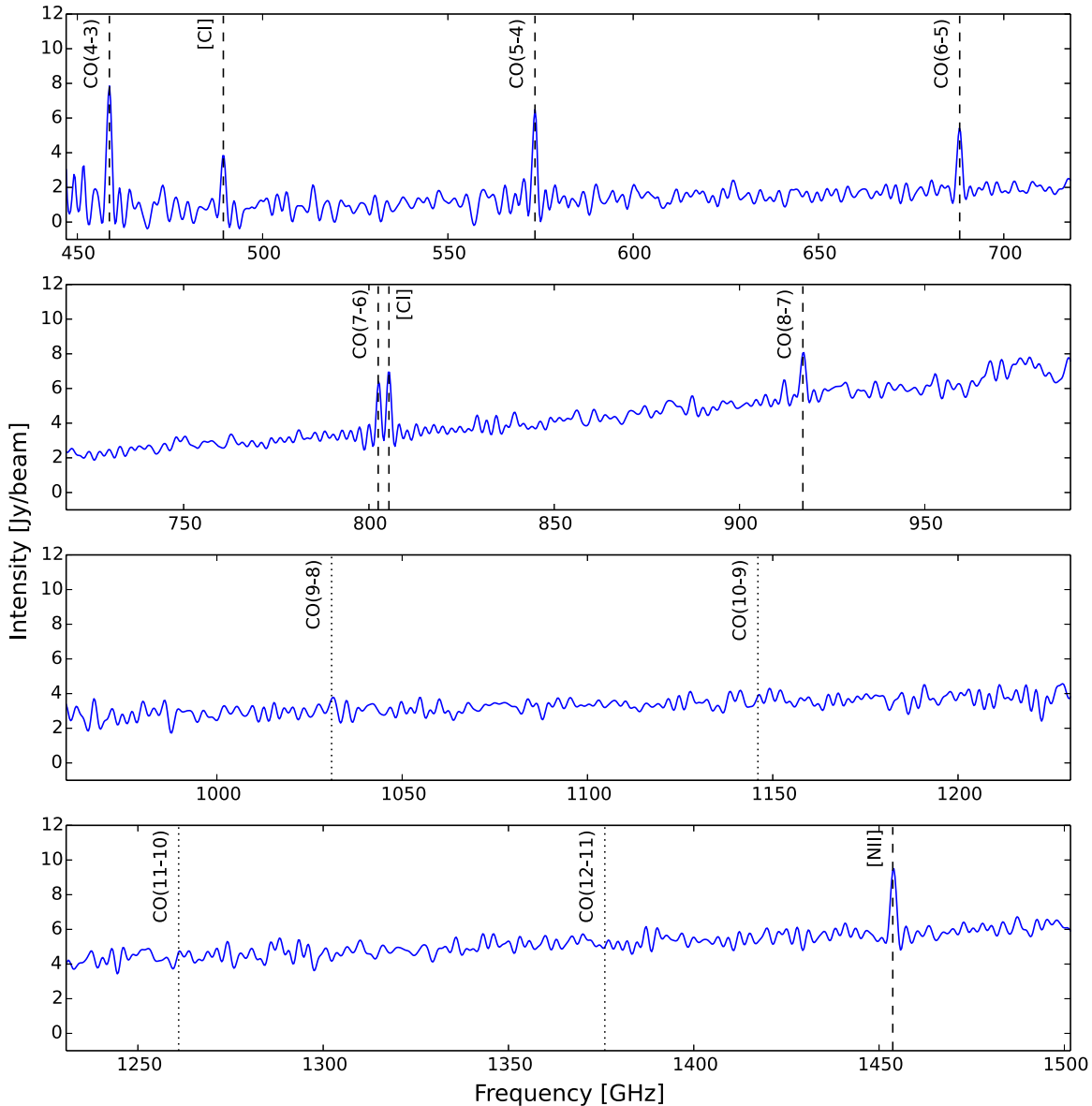

Figure 2. FTS spectrum for the overlap region covering the entire spectral range of the FTS. This position corresponds to the blue box in Figure 5. The top two panels correspond to the SLW and the bottom two panels correspond to the SSW, while the jump in the continuum between the second and third panels from the top is due to the large difference in beam size between the SLW ($\sim 37''$) and the SSW ($\sim 21''$) at the junction. The dashed lines indicate the detected and identified molecular and atomic transitions while the dotted lines indicate where we would expect to find the undetected higher J CO transitions.

(A color version of this figure is available in the online journal.)

The resulting map is Nyquist-sampled and covers the entire CO-emitting region with a total area of $140'' \times 140''$ and a total integration time of 14,940 s. The main-beam efficiency was $\eta_{MB} = 0.69$ and the beam size was $20''\!.8$ at 230.56 GHz. The JCMT CO $J = 3$–2 observations were obtained as part of project M09BC05 (PI: Tara Parkin) on 2009 December 10, 16, and 17. The beam size of the telescope was $14''\!.5$. We obtained a raster map over an area of $159'' \times 186''$ in position-switched mode with a total integration time of 2111 s and we used a bandwidth of 1 GHz across 2048 channels. We reduce both data sets using the methods described in Warren et al. (2010) and Parkin et al. (2012) using the `Starlink` software package, with the exception that we convolve the maps using custom convolution kernels described in Section 2.3 rather than a Gaussian kernel.

2.2.3. [C II] 158 μm and [O I] 63 μm

The [C II] 158 μm and [O I] 63 μm transitions were observed in the Antennae using the *Herschel* PACS instrument, each in three separate pointings: one centered on each of the nuclei of NGC 4038 (Observation IDs 1342199405 and 1342199406), NGC 4039 (Observation IDs 1342210820 and 1342210821), and the overlap region (Observation IDs 1342210822 and 1342210823). All of these observations were performed in a single pointing in chopping-nodding mode. The field of view for each observation is $47'' \times 47''$ and all observations were binned to a $3''$ pixel size. The beam sizes and spectral resolution were $\sim 11''$ and 239 km s^{-1} for [C II] 158 μm and $\sim 9''$ and 98 km s^{-1} for [O I] 63 μm (PACS observers manual version 2.5.1[11]).

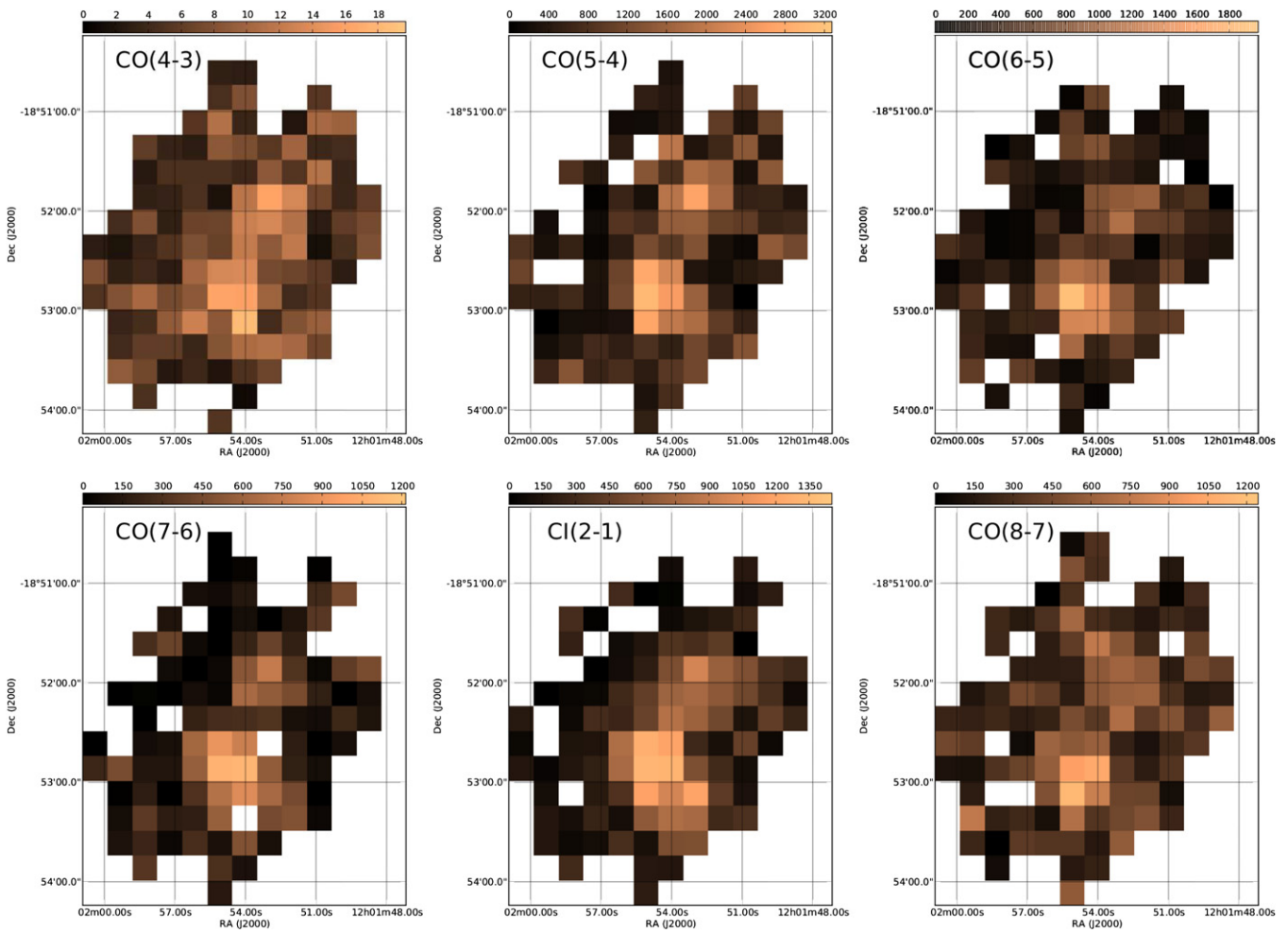[11] Available at http://herschel.esac.esa.int/Docs/PACS/html/pacs_om.html.

Figure 3. Integrated intensity maps for the SPIRE-FTS CO and [C I] emission lines in units of Jy km s^{-1}. These maps are at the instrument resolution. The [C I] 1–0 line map is shown in Figure 5.

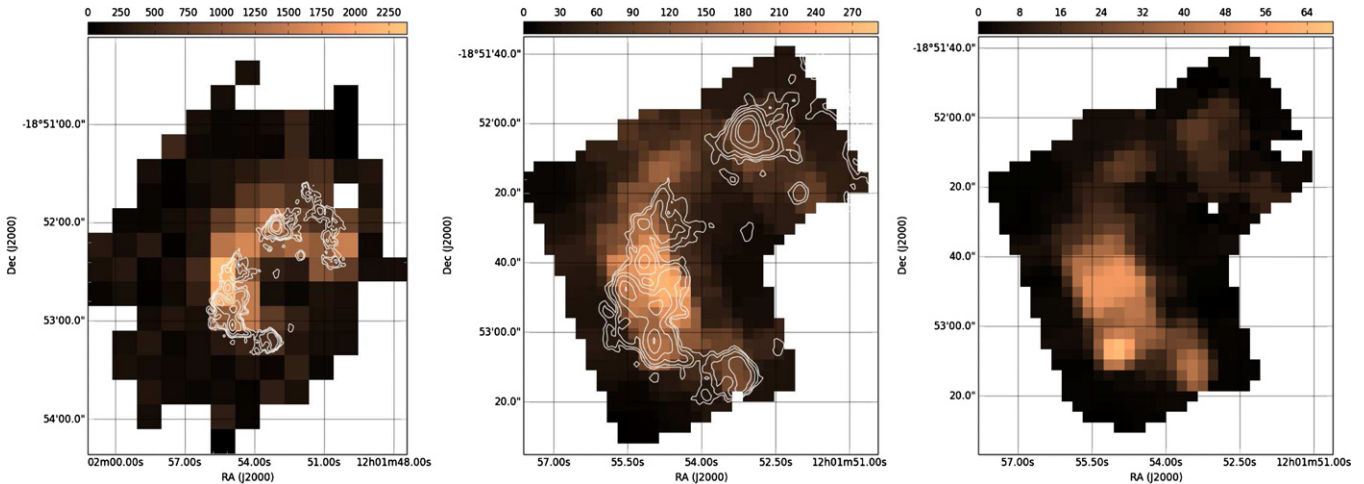(A color version of this figure is available in the online journal.)

Figure 4. Integrated intensity maps for the [N II] 205 μm (left), [C II] 158 μm (center), and [O I] 63 μm (right) atomic fine structure lines at the instrument resolution. The [N II] map is in units of Jy beam^{-1} km s^{-1}, while the [C II] and [O I] maps are in units of Jy sr^{-1} km s^{-1}. The CO $J = 1$–0 contours from Wilson et al. (2003) are overlaid in white on the [N II] and [C II] images, with the contours corresponding to 1%, 2.5%, 6% 15%, 37%, and 57% of the peak intensity.

(A color version of this figure is available in the online journal.)

The level 2 data cubes were obtained from the *Herschel* Science Archive on 2012 October 10 ([C II] 158 μm) and 2012 December 12 ([O I] 63 μm). For each data cube, we fit and subtract the baseline in each pixel with a first-order polynomial before fitting the line with a Gaussian. We create an integrated intensity map for each transition by integrating across the fitted

Table 1
Line Flux Measurements

Line	Rest Frequency (GHz)	NGC 4038 (K km s^{-1})	Overlap Region (K km s^{-1})	NGC 4039 (K km s^{-1})	Calibration Uncertainty (%)
CO $J = 1$–0	115.27	23.1	42.3	19.6	20
CO $J = 2$–1	230.54	20.6 ± 0.4	40.0 ± 0.4	25.6 ± 0.4	15
CO $J = 3$–2	345.80	15.0 ± 0.3	28.7 ± 0.4	15 ± 1	15
CO $J = 4$–3	461.04	16 ± 1	16.4 ± 0.2	8.5 ± 0.8	12
CO $J = 5$–4	576.28	4.5 ± 0.4	6.0 ± 0.5	3.4 ± 0.6	12
CO $J = 6$–5	691.47	2.5 ± 0.3	4.5 ± 0.3	3.0 ± 0.2	12
CO $J = 7$–6	806.65	0.8 ± 0.2	1.3 ± 0.4	1.0 ± 0.2	12
CO $J = 8$–7	921.80	0.7 ± 0.1	0.9 ± 0.1	0.55 ± 0.07	12
[C I] $J = 1$–0	492.16	2.4 ± 0.4	5.7 ± 0.1	4.0 ± 0.5	12
[C I] $J = 2$–1	809.34	1.0 ± 0.2	1.7 ± 0.4	1.3 ± 0.2	12
[N II][a]	1461.13	2.9 ± 0.2	2.20 ± 0.04	1.09 ± 0.03	12

Note. [a] Measurements for [N II] are from the unconvolved map (beam size $\sim 17''$). All other measurements are at a beam size of $43''$.

Gaussian in each pixel. For each transition, we combine the three maps using *wcsmosaic* in the `Starlink` software package. The resulting maps are shown in Figure 4.

2.3. Convolution

The FTS beam size and shape varies across both the SLW and SSW, from $\sim 17''$ to $\sim 43''$ (SPIRE Observers' Manual version 2.4; Swinyard et al. 2010), with the largest beam size occurring at the low-frequency end of the SLW. We developed convolution kernels using the method described in Bendo et al. (2012) for the ground-based observations of the CO $J = 1$–0, $J = 2$–1, and $J = 3$–2 transitions and for the SPIRE observations of the $J = 5$–4 to 8–7 transitions to match the CO $J = 4$–3 beam ($\sim 43''$). The kernels for the SPIRE CO transitions are the same kernels used in Kamenetzky et al. (2012) and Spinoglio et al. (2012). We use the CO $J = 7$–6 kernel to convolve the [C I] $J = 2$–1 map. Finally, we convert from Jy beam^{-1} km s^{-1} to K km s^{-1} using

$$I_{ij} = S_{ij} \left[0.0109 \theta_{ij}^2 \left(\frac{\nu_{ij}}{115} \right)^2 \right]^{-1}, \qquad (1)$$

where ν_{ij} is the frequency of the transition in GHz, θ_{ij} is the FWHM beam size in arcseconds, I_{ij} is the integrated intensity in units of K km s^{-1}, and S_{ij} is in units of Jy beam^{-1} km s^{-1}. We use a beam size of $43''.4$ for the convolved maps. The convolved maps are shown in Figure 5, while the integrated intensities for the nuclei of NGC 4038 and NGC 4039 and the overlap region are given in Table 1 in units of K km s^{-1}.

3. RADIATIVE TRANSFER ANALYSIS

3.1. [C I] Local Thermodynamic Equilibrium Analysis

In this section, we calculate the temperature of the gas using the two [C I] lines, $^3P_1$–$^3P_0$ and $^3P_2$–$^3P_1$, assuming local thermodynamic equilibrium (LTE). We calculate the kinetic temperature using a rewritten version of Equation (3) from Spinoglio et al. (2012):

$$T_{\text{kin}} = -\frac{E_{21}}{k} \left[\ln \left(\frac{g_1}{g_2} \frac{A_{10} \nu_{21}^2 I_{21}}{A_{21} \nu_{10}^2 I_{10}} \right) \right]^{-1}, \qquad (2)$$

where ν_{ij} is the frequency of the transition in GHz, I_{ij} is the integrated intensity in units of K km s^{-1}, A_{ij} is the Einstein

coefficient, and γ_{ij} is the collisional rate. We use the values of $A_{10} = 7.93 \times 10^{-8}$ s^{-1}, $A_{20} = 2 \times 10^{-14}$ s^{-1}, and $A_{21} = 2.68 \times 10^{-7}$ s^{-1} for the Einstein coefficients (Papadopoulos et al. 2004). For the collisional rate coefficients, we assume a temperature of 30 K and an ortho-to-para ratio of 3 and, using the tabulated data from Schroder et al. (1991), calculate $\gamma_{10} = 1.3 \times 10^{-10}$ cm^3 s^{-1}, $\gamma_{20} = 6.9 \times 10^{-11}$ cm^3 s^{-1}, and $\gamma_{21} = 8.3 \times 10^{-11}$ cm^3 s^{-1}.

We calculate the temperature in all pixels in our map where we detect both [C I] transitions (Figure 6). Our results suggest that the majority of the [C I] emission is associated with cold molecular gas with temperatures of ~ 10–30 K.

3.2. Non-LTE Analysis

We model the CO and [C I] emission using the non-LTE code RADEX (van der Tak et al. 2007), available from the Leiden Atomic and Molecular Database (LAMDA; Schöier et al. 2005). RADEX iteratively solves for statistical equilibrium based on three input parameters: the molecular gas density ($n(H_2)$), the column density of the molecular species of interest (N_{mol}), and the kinetic temperature of the molecular gas (T_{kin}). From these three input parameters, RADEX will calculate the line fluxes and optical depths for any molecular or atomic species for which basic molecular data, including the energy levels, Einstein A-coefficients, and collision rates, are known. Molecular data files are available from LAMDA.

We calculate a grid of CO fluxes and optical depths with RADEX spanning a large parameter space in density, temperature, and column density per unit line width ($N_{\text{mol}}/\Delta V$) using the uniform sphere approximation. In addition, we calculate a secondary grid of [C I] fluxes and optical depths based on the same parameter space while varying the [C I] abundance relative to CO ($x_{[C I]}/x_{CO}$). The Antennae itself is significantly more complex than a simple uniform sphere; however, our results are averaged over the entire FTS beam. The complete list of grid parameters is shown in Table 2.

3.2.1. Likelihood Analysis

We used a Bayesian likelihood code (Ward et al. 2003; Naylor et al. 2010a; Panuzzo et al. 2010; Kamenetzky et al. 2011) to determine the most likely solutions for the physical state of the molecular gas for a given set of measured CO and [C I] line-integrated intensities. We list the highlights of the code here, while further details can be found in Kamenetzky et al. (2012). The likelihood code includes an area filling factor (Φ_A)
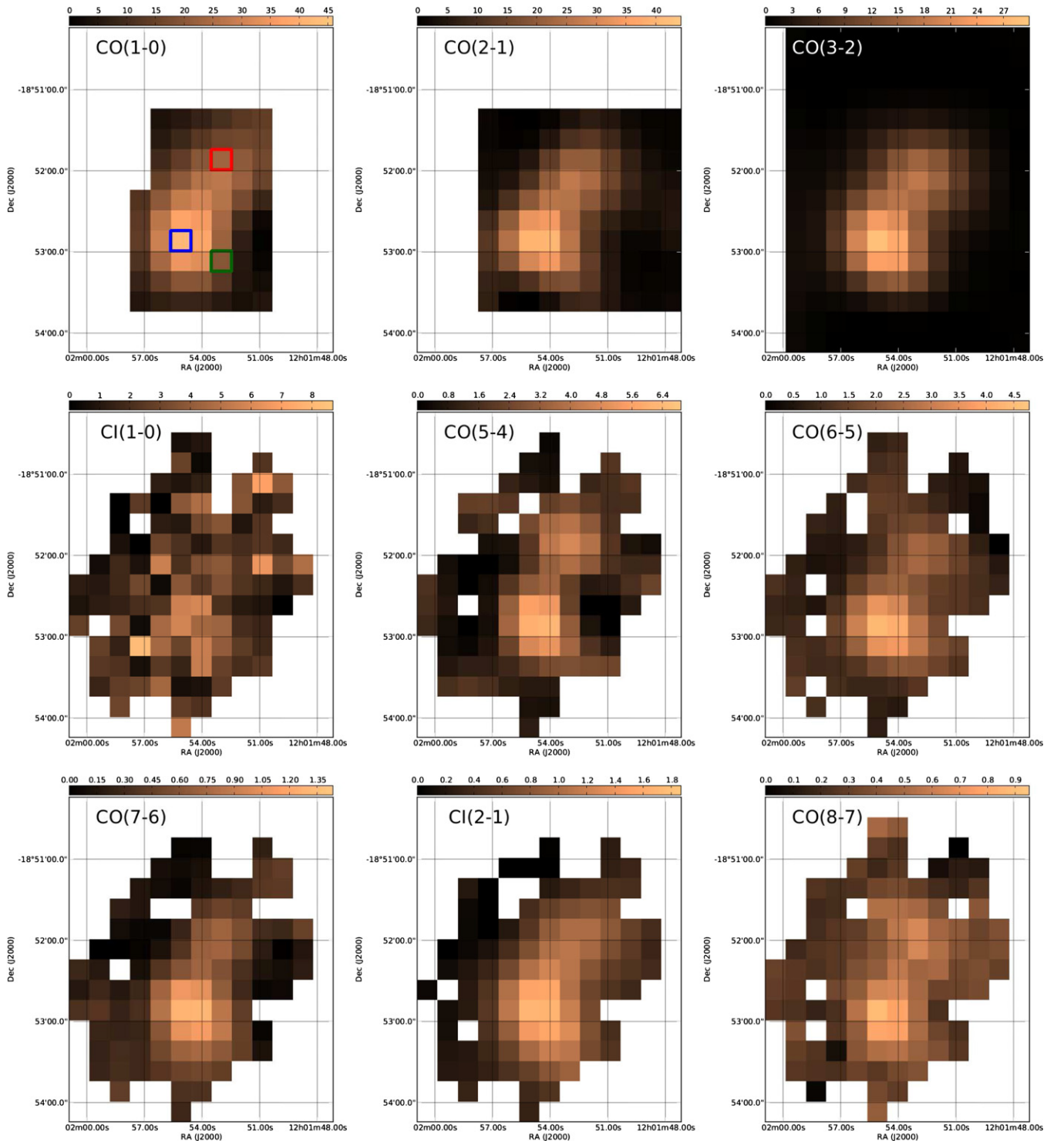
Figure 5. Convolved integrated intensity maps for CO and [C I] in units of K km s^{-1}. The CO $J = 1$–0 observations are from the NRO (Zhu et al. 2003), while the CO $J = 2$–1 and $J = 3$–2 observations are from the JCMT. All other observations are from the SPIRE-FTS. All of these maps except for the [C I] $J = 1$–0 maps have been convolved to match the largest beam size of the FTS at 43″. The red, blue, and green squares on the CO $J = 1$–0 map indicate the location of NGC 4038, the overlap region, and NGC 4039 (see Figure 1 for beam location). The CO $J = 4$–3 image is shown in Figure 3.

(A color version of this figure is available in the online journal.)

with the RADEX grid parameters (T_{kin}, $n(H_2)$, and $N_{CO}/\Delta V$) to create a four-dimensional (4D) parameter space. Assuming Bayes' theorem, the code compares the measured fluxes with those in our RADEX grid to calculate the probability that a given set of parameters produces the observed set of emission lines. In addition, the source line width (ΔV) is included as

an input parameter in order to properly compare measured and calculated integrated intensities. We use the convolved CO $J = 3$–2 second-moment map for the source line widths of each pixel in our maps.

The code calculates three values for each parameter: the median, the 1DMax, and the 4DMax. The 1DMax corresponds
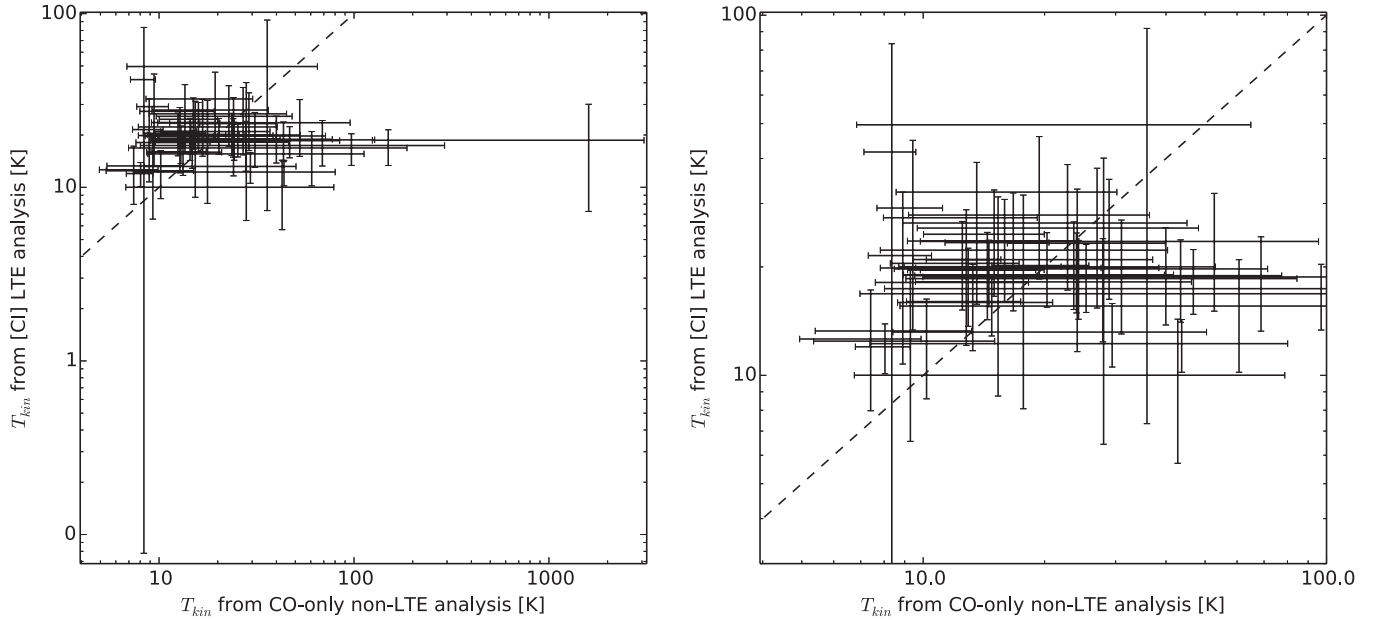
Figure 6. Left: cold molecular gas temperature from the [C I] LTE analysis (*y*-axis) and the CO-only non-LTE radiative transfer analysis (*x*-axis). Right: zoom-in on the upper left portion of the left panel. The error bars correspond to the 1σ uncertainty in the respective temperatures. Note that where the error bars cross corresponds only to the midpoint of the 1σ ranges in log space and not to the most probable value. The dashed diagonal line corresponds to where the two temperature are equal.

Table 2
RADEX Grid Parameters

Parameter	Range	Number of Points
T_{kin} (K)	$10^{0.7}$–$10^{3.8}$	71
$n(\mathrm{H_2})\,(\mathrm{cm^{-3}})$	$10^{1.0}$–$10^{7.0}$	71
Φ_A	$10^{-5.0}$–1	71
$N_{\mathrm{CO}}/\Delta V\,(\mathrm{cm^{-2}})$	$10^{12.0}$–$10^{18.0}$	81
$N_{\mathrm{[C\,I]}}/N_{\mathrm{CO}}$	$10^{-2.0}$–$10^{2.0}$	20
$\Delta V\,(\mathrm{km\,s^{-1}})$	1.0	

Note. Column density is calculated per unit line width, while the line width is held fixed at $1\,\mathrm{km\,s^{-1}}$ in the grid calculations (see the text).

Table 3
Model Constraints

Parameter	Value	Units
CO abundance (x_{CO})	3×10^{-4}	. . .
Mean molecular weight (μ)	1.5	. . .
Angular size scale	107	pc arcsec^{-1}
Source size	43	$''$
Length (L)	$\leqslant 1930^{\mathrm{a}}$	pc
Dynamical mass (M_{dyn})	$\leqslant 3.1 \times 10^{9\mathrm{b}}$	$M_{\odot}$

Notes.
[a] Physical size of the nucleus of NGC 4038 from Wilson et al. (2000) corrected to a distance of 22 pc.
[b] Sum of the virial masses of all SGMCs in the overlap region from Wilson et al. (2003), corrected for incompleteness; see the text.

to the most probable value for the given parameter based upon the one-dimensional (1D) likelihood distribution for that parameter, while the median is also calculated from the 1D likelihood distribution. The 4DMax is only calculated explicitly for the four grid parameters (T_{kin}, $n(\mathrm{H_2})$, N_{CO}, Φ_A) and is the most probable set of values based upon the 4D likelihood distribution of the four parameters. Finally, the 1σ range is calculated from the 1D likelihood distribution.

We use three priors to constrain our solutions to those that are physically realizable (Ward et al. 2003; Rangwala et al. 2011). The first prior places a limit on the column density, ensuring that the total mass in the column does not exceed the dynamical mass of the system, or

$$N_{\mathrm{CO}} < \frac{M_{\mathrm{dyn}} x_{\mathrm{CO}}}{\mu m_{\mathrm{H_2}} A_{\mathrm{CO}} \Phi_A}, \qquad (3)$$

where μ is the mean molecular weight, M_{dyn} is the dynamical mass of the system, x_{CO} is the CO abundance relative to H_2, and A_{CO} is the area of the CO-emitting region. The dynamical mass is calculated as the sum of the virial masses of all of the SGMCs in the overlap region from Wilson et al. (2000), corrected for incompleteness as some of the mass will be found in unresolved SGMCs (e.g., see Wilson et al. 2003).

This incompleteness correction is performed by calculating the fraction of CO emission in unresolved SGMCs in the overlap region. The corrected dynamical mass is $3.1 \times 10^9\,M_{\odot}$. While the dynamical mass in other parts of the galaxy will be less than in the overlap region (e.g., see Zhu et al. 2003), it is very difficult to determine how much mass is observed by each pixel in our maps. Therefore, we conservatively use the highest possible mass we expect in the beam for one pixel. Using these values along with those listed in Table 3, we limit the product of the column density and filling factor to

$$N_{\mathrm{CO}} \Phi_A < 10^{18.36}\,\mathrm{cm^{-2}}. \qquad (4)$$

The second prior limits the total length of the column to be less than the length of the molecular region on the plane of the sky, so that

$$\frac{N_{\mathrm{CO}}}{\sqrt{\Phi_A} x_{\mathrm{CO}} n(\mathrm{H_2})} \leqslant L, \qquad (5)$$

where L is the size of the CO-emitting region. We use the diameter of the nucleus of NGC 4038 ($L = 1900$ pc) from Wilson et al. (2000), corrected to a distance of 22 Mpc, since it

is the largest single molecular complex in the Antennae. As such, this provides an upper limit on the true size of CO, regardless of which pixel is being considered. All of the physical parameters used to calculate the first two priors are listed in Table 3.

The third prior limits the optical depth to be $-1 < \tau < 100$, as recommended by the RADEX documentation (van der Tak et al. 2007). A negative optical depth is indicative of a "maser," which is nonlinear amplification of the incoming radiation. RADEX cannot accurately calculate the line intensities when the optical depth is less than $\tau < -1$ and masing is not expected, so these solutions should be disregarded. Conversely, a high optical depth can lead to unrealistically high calculated temperatures and so should be disregarded and, in any case, our models do not approach that high optical depth limit.

3.3. RADEX Results

3.3.1. CO Only

We model the CO emission for each pixel in our map where we have a detection for all eight of our observed CO transitions ($J = 1$–0 to $J = 8$–7) and both [C I] transitions. The pixels associated with NGC 4038, NGC 4039, and the overlap region are shown on the CO $J = 1$–0 map in Figure 5, while the beams associated with these pixels are shown in Figure 1. We assume that all of the molecular gas in each pixel is in one of two distinct components:[12] a cold component and a warm component. Studies of the Antennae have revealed that there is both cold gas (e.g., Wilson et al. 2000; Zhu et al. 2003) and warm gas (e.g., Brandl et al. 2009; Herrera et al. 2012); however, the molecular gas likely populates a spectrum of temperature and density ranges. While a two-component model is unlikely to represent the true physical state of the molecular gas, it does provide us with an average, along with a statistical range, of the temperature, density, and column density of the molecular gas.

Under the two-component assumption, the cold component dominates the lower J CO emission while the warm component dominates the higher J CO emission. We begin by fitting the cold component to the lower J lines up to some transition $J_{up} \leqslant J_{break}$ and setting the measurements of the higher transitions ($J_{up} > J_{break}$) as upper limits. We subtract the resulting calculated cold component from the line fluxes and fit the residual high J CO emission as a "warm component," while keeping the residuals of the lower J CO transitions as upper limits. Following this fit, we subtract the warm component from our measured data and fit the cold component once again. We continue to iterate in this manner until we converge upon a set of solutions. We solve for values of $J_{break} = 3$, 4, and 5 and present a χ^2 goodness-of-fit parameter for each solution in Table 4. For the overlap region and NGC 4038, the $J_{break} = 3$ solution presents the worst fit, while the differences between the $J_{break} = 4$ and $J_{break} = 5$ solutions are minimal. Furthermore, for NGC 4039, all three solutions present reasonable fits with

---

[12] We performed one-component fits in NGC 4038, NGC 4039, and the overlap region both with and without the two [C I] transitions in addition to our eight CO transitions. In all three cases, we recovered only warm ($T_{kin} \gtrsim 100$ K), low-density ($n(H_2) \lesssim 10^3$ cm^{-3}) molecular gas. Furthermore, we recovered a molecular gas mass of $M_{beam} \sim 10^8 M_\odot$ or less in all three regions, which leads to a total molecular gas mass $\sim$ a few $10^8 M_\odot$ for the entire galaxy (assuming a CO abundance of 3×10^{-4}). CO $J = 1$–0 interferometric observations from Wilson et al. (2000) found that, in all three regions, the amount of molecular gas exceeds $5.0 \times 10^8 M_\odot$ using two methods. Given the warm temperatures and low density of the gas we recovered with our one-component fit, along with the low molecular gas mass, we feel that the one-component fit does not represent a physical solution.

Table 4
χ^2 Values of Two-component Fit for Various J_{break}

Model	J_{break}	NGC 4038		Overlap Region		NGC 4039	
		χ^2_{CO}	$\chi^2_{[C I]}$	χ^2_{CO}	$\chi^2_{[C I]}$	χ^2_{CO}	$\chi^2_{[C I]}$
CO only	3	31.2	...	27.7	...	**5.5**	
	4	12.2	...	**10.7**	...	13.1	
	5	**11.9**	...	16.0	...	15.3	
CO and [C I]	3	37.6	663.5	30.5	2431.9	**5.4**	969.7
	4	**10.2**	**4.8**	**22.2**	**1.2**	20.4	**2.2**
	5	10.4	**4.8**	25.5	3.9	10.1	563.6

Note. The best χ^2 for each position is highlighted in bold.

the $J_{break} = 3$ solution producing the best fit. Therefore, for consistency, we report the $J_{break} = 4$ solution for each pixel in our map; however, it is important to note that the statistical ranges in the physical parameters for all three solutions do not depend appreciably on the value of J_{break}.

The measured and calculated CO spectral line energy distributions (SLEDs) are shown in Figure 7 while the optical depths are shown in Figure 8, both calculated from the 4DMax solutions (see Tables 5 and 6). In NGC 4038 and the overlap region, the cold component dominates the emission for all transitions where $J_{upper} \leqslant 5$, while the warm component is dominant only for the two highest J CO transitions. In NGC 4039, the cold component dominates only for the $J_{upper} \leqslant 4$ transitions. In all cases, the warm component is more optically thin than the cold component for almost all of the CO transitions (Figure 8).

The fitted physical parameters for NGC 4038, the overlap region, and NGC 4039 are shown in Tables 5 (cold component) and 6 (warm component). In all three regions, the upper limits of the density for both the cold and warm components are not well constrained (Figure 9, top). As a result, the upper limit on the pressure, which is the product of the temperature and density, is not well constrained. The 1σ range of the temperature of the cold component in all three regions is constrained to being cold ($T_{kin} \lesssim 40$ K), which agrees well with our [C I] LTE analysis (Figure 6). The filling factor and the CO column density for the cold component in all three regions is well constrained (Figure 9, bottom). The lack of constraint for the warm components of these three regions can be attributed to the degeneracy of Φ_A and N_{CO} (e.g., see Kamenetzky et al. 2012). Their product, which is equal to the beam-averaged column density ($\langle N_{CO} \rangle$), is well constrained for both the warm and cold component in all three regions (Figure 9, bottom). If we assume that the CO abundance (x_{CO}) is the same for both the warm and cold component, the warm component would correspond to $\sim$0.1%–0.3% of the total molecular gas mass in the nucleus of NGC 4038 and the overlap region and $\sim$1% of the total gas mass in the nucleus of NGC 4039.

Results for the entire system are shown in Figure 10. In this figure, it is important to note that, since our pixel size (15″) is less than our beam size ($\sim$43″), data points on these plots are not entirely independent. We compare the 1σ ranges for the temperature (top row) and beam-averaged column density (bottom row) to those for the density (left column) and pressure (right column). Both a cold and warm component are revealed outside of NGC 4038, NGC 4039, and the overlap region (Figure 10, top row). Furthermore, no distinction can be made between the density of the cold and warm components (Figure 10, left column). The pressure in each of the cold and warm components does not vary by more than $\sim$1–2 orders of
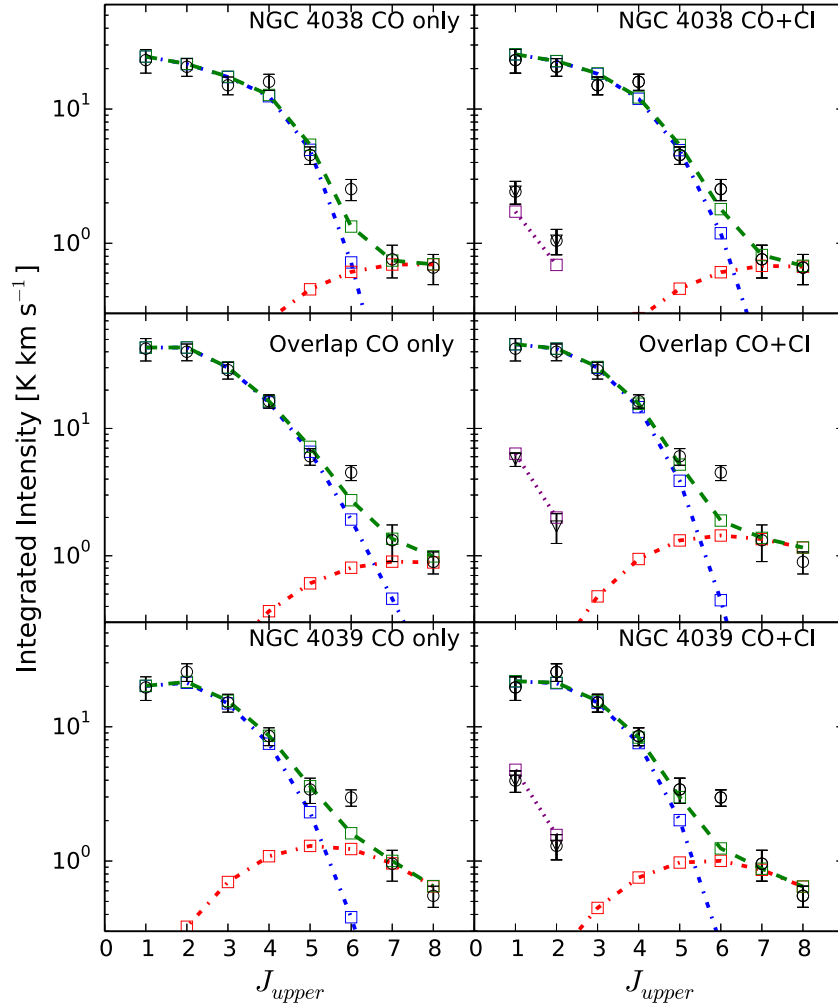
Figure 7. Measured and calculated CO SLEDs for the nucleus of NGC 4038 (top), the overlap region (middle), and the nucleus of NGC 4039 (bottom) and for $J_{\rm break} = 4$. The left panels correspond to solutions including only CO while the right panels correspond to solutions including both CO and [C I]. In all panels, the blue dashed-dotted line and squares correspond to the cold component, the red dashed-dotted line and squares correspond to the warm component, the green dashed line and squares represent the sum of the cold and warm component, and the black circles correspond to the measured CO data. In the right column, the purple dotted line and squares correspond to the calculated [C I] flux while the black triangles correspond to the measured [C I] flux.

(A color version of this figure is available in the online journal.)

Table 5
Cold Component Likelihood Results: CO Only

| Source	Parameter	Median	1σ Range	1D Max	4D Max	Unit
NGC 4038	$T_{\rm kin}$	13	10–20	12	14	(K)
	$n({\rm H_2})$	$10^{4.97}$	$10^{3.73}$–$10^{6.33}$	$10^{4.00}$	$10^{5.54}$	(cm^{-3})
	$N_{\rm CO}$	$10^{18.95}$	$10^{18.53}$–$10^{19.49}$	$10^{18.80}$	$10^{18.72}$	(cm^{-2})
	Φ_A	$10^{-1.80}$	$10^{-2.02}$–$10^{-1.62}$	$10^{-1.71}$	$10^{-1.79}$	
	P	$10^{6.05}$	$10^{5.01}$–$10^{7.39}$	$10^{5.47}$	$10^{5.47}$	(K cm^{-2})
	$\langle N_{\rm CO} \rangle$	$10^{17.24}$	$10^{16.71}$–$10^{17.76}$	$10^{17.33}$	$10^{17.33}$	(cm^{-2})
Overlap region	$T_{\rm kin}$	15	10–38	12	63	(K)
	$n({\rm H_2})$	$10^{4.16}$	$10^{3.23}$–$10^{6.01}$	$10^{3.40}$	$10^{3.40}$	(cm^{-3})
	$N_{\rm CO}$	$10^{18.91}$	$10^{18.35}$–$10^{19.55}$	$10^{18.62}$	$10^{18.70}$	(cm^{-2})
	Φ_A	$10^{-1.66}$	$10^{-1.94}$–$10^{-1.42}$	$10^{-1.50}$	$10^{-1.93}$	
	P	$10^{5.37}$	$10^{4.66}$–$10^{7.02}$	$10^{5.22}$	$10^{5.22}$	(K cm^{-2})
	$\langle N_{\rm CO} \rangle$	$10^{17.34}$	$10^{16.72}$–$10^{17.99}$	$10^{16.87}$	$10^{16.87}$	(cm^{-2})
NGC 4039	$T_{\rm kin}$	15	10–37	12	28	(K)
	$n({\rm H_2})$	$10^{4.27}$	$10^{3.33}$–$10^{6.07}$	$10^{3.49}$	$10^{3.83}$	(cm^{-3})
	$N_{\rm CO}$	$10^{18.72}$	$10^{18.13}$–$10^{19.48}$	$10^{18.61}$	$10^{18.76}$	(cm^{-2})
	Φ_A	$10^{-2.00}$	$10^{-2.26}$–$10^{-1.75}$	$10^{-1.93}$	$10^{-2.21}$	
	P	$10^{5.46}$	$10^{4.82}$–$10^{7.11}$	$10^{5.22}$	$10^{5.22}$	(K cm^{-2})
	$\langle N_{\rm CO} \rangle$	$10^{16.75}$	$10^{16.24}$–$10^{17.55}$	$10^{16.49}$	$10^{16.49}$	(cm^{-2})
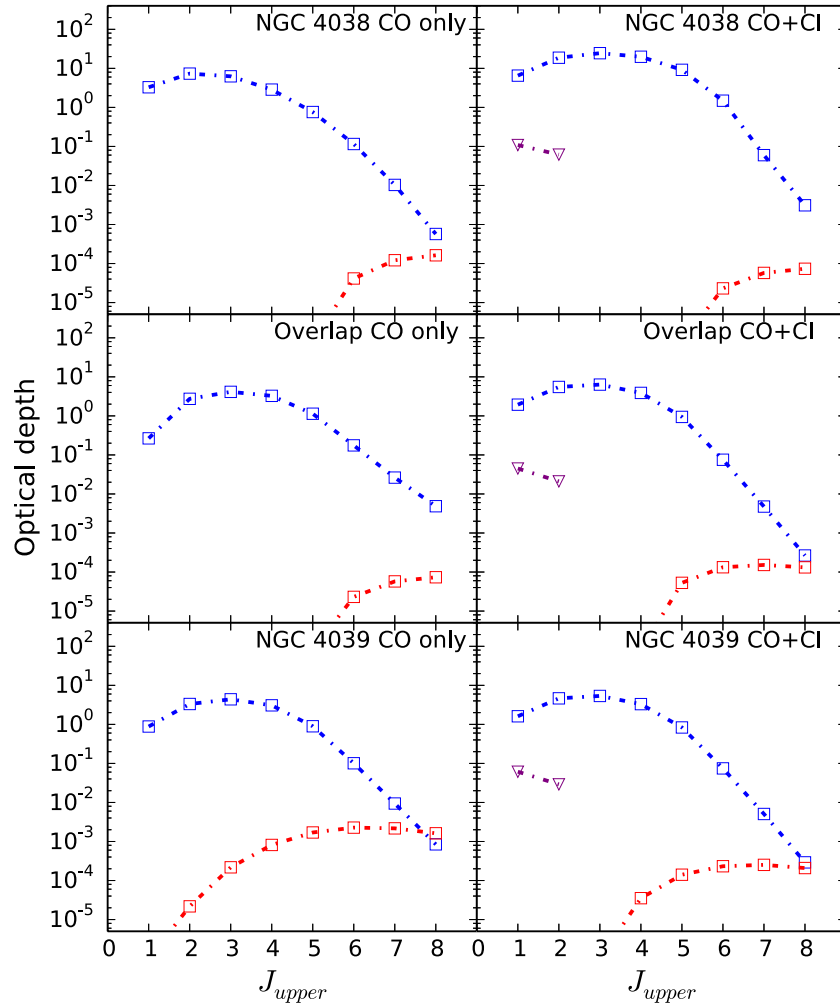
Figure 8. Best-fit model CO optical depth for the nucleus of NGC 4038 (top), the overlap region (middle), and the nucleus of NGC 4039 (bottom) and for $J_{break} = 4$. The left panels correspond to solutions including only CO while the right panels correspond to solutions including both CO and [C I]. In all panels, the blue dashed-dotted line and squares correspond to the cold component and the red dashed-dotted line and squares correspond to the warm component. In the right column, the purple dotted line and squares correspond to the calculated [C I] optical depth. The warm component CO emission and the [C I] emission are optically thin.

(A color version of this figure is available in the online journal.)

Table 6
Warm Component Likelihood Results: CO Only

| Source	Parameter	Median	1σ Range	1D Max	4D Max	Unit
NGC 4038	T_{kin}	1071	368–3361	647	5997	(K)
	$n(H_2)$	$10^{5.73}$	$10^{4.75}$–$10^{6.60}$	$10^{7.00}$	$10^{4.26}$	(cm^{-3})
	N_{CO}	$10^{17.04}$	$10^{15.30}$–$10^{18.83}$	$10^{16.17}$	$10^{15.05}$	(cm^{-2})
	Φ_A	$10^{-2.55}$	$10^{-4.27}$–$10^{-0.81}$	$10^{-4.57}$	$10^{-0.71}$	
	P	$10^{9.28}$	$10^{8.15}$–$10^{10.21}$	$10^{9.44}$	$10^{9.44}$	(K cm^{-2})
	$\langle N_{CO} \rangle$	$10^{14.47}$	$10^{14.23}$–$10^{14.85}$	$10^{14.43}$	$10^{14.43}$	(cm^{-2})
Overlap region	T_{kin}	732	279–2790	389	3999	(K)
	$n(H_2)$	$10^{5.57}$	$10^{4.56}$–$10^{6.55}$	$10^{4.43}$	$10^{4.26}$	(cm^{-3})
	N_{CO}	$10^{17.08}$	$10^{15.32}$–$10^{18.90}$	$10^{15.92}$	$10^{14.80}$	(cm^{-2})
	Φ_A	$10^{-2.59}$	$10^{-4.32}$–$10^{-0.82}$	$10^{-4.79}$	$10^{-0.36}$	
	P	$10^{8.92}$	$10^{7.86}$–$10^{9.95}$	$10^{7.90}$	$10^{7.90}$	(K cm^{-2})
	$\langle N_{CO} \rangle$	$10^{14.48}$	$10^{14.27}$–$10^{14.79}$	$10^{14.41}$	$10^{14.41}$	(cm^{-2})
NGC 4039	T_{kin}	324	123–1276	212	234	(K)
	$n(H_2)$	$10^{4.51}$	$10^{4.00}$–$10^{5.22}$	$10^{4.34}$	$10^{4.69}$	(cm^{-3})
	N_{CO}	$10^{16.34}$	$10^{15.11}$–$10^{17.66}$	$10^{15.68}$	$10^{16.06}$	(cm^{-2})
	Φ_A	$10^{-1.86}$	$10^{-3.16}$–$10^{-0.63}$	$10^{-1.07}$	$10^{-1.43}$	
	P	$10^{7.13}$	$10^{6.95}$–$10^{7.49}$	$10^{7.13}$	$10^{7.13}$	(K cm^{-2})
	$\langle N_{CO} \rangle$	$10^{14.49}$	$10^{14.40}$–$10^{14.64}$	$10^{14.61}$	$10^{14.61}$	(cm^{-2})

11
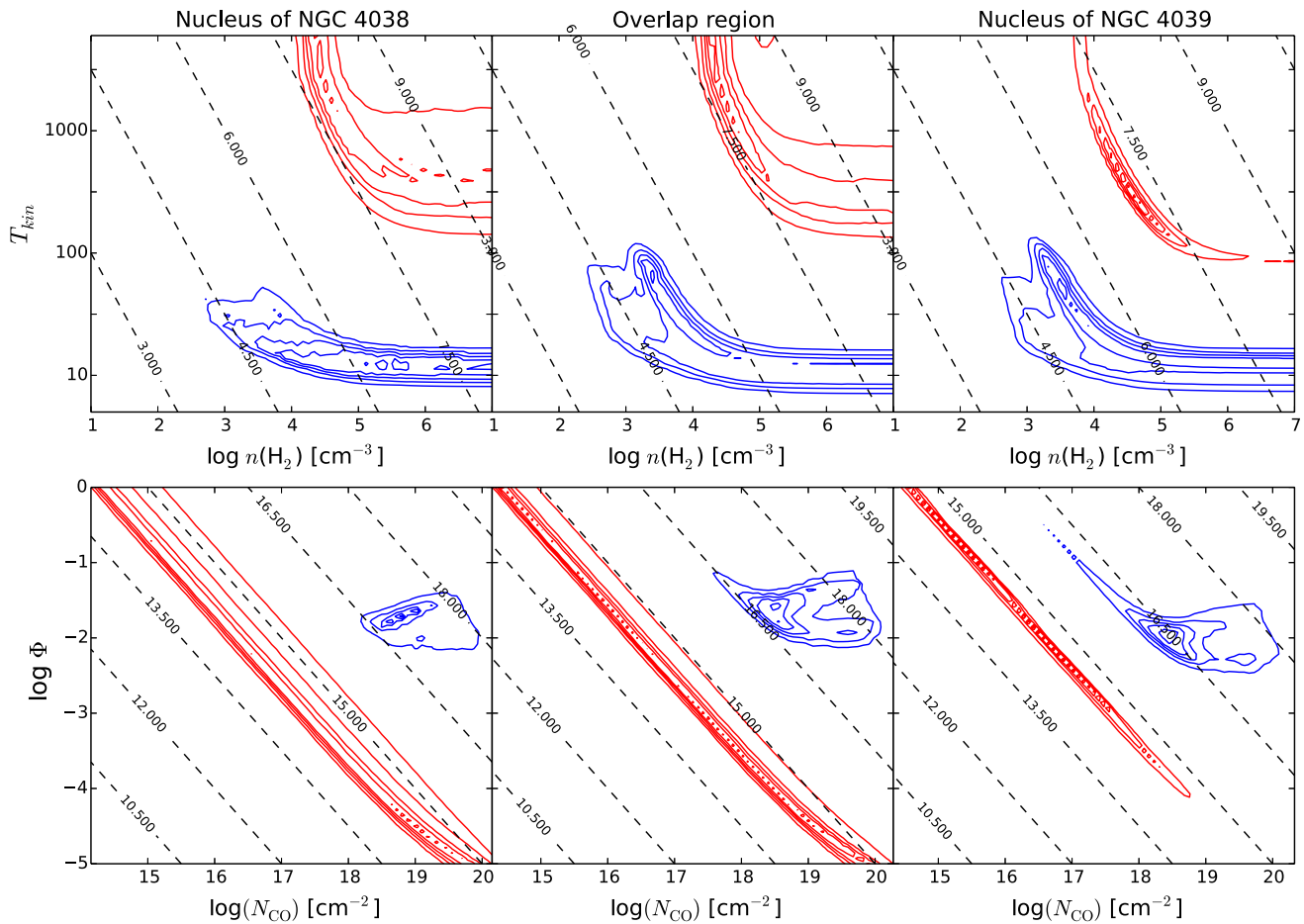
Figure 9. Contour probability plots for the CO-only solutions with $J_{\rm break} = 4$ for the warm (red contours) and cold (blue contours) in the nucleus of NGC 4038 (left), the overlap region (middle), and the nucleus of NGC 4039 (right) and for kinetic temperature and density (top) and the filling factor and column density (bottom). The dashed diagonal lines correspond to the logarithm of the pressure in units of Log(K cm^{-2}) (top) and the beam-averaged column density, denoted as $\langle N_{\rm CO} \rangle$ in the tables, in units of Log(cm^{-2}) (bottom). The contours correspond to 10%, 30%, 50%, 70%, and 90% peak probability.

(A color version of this figure is available in the online journal.)

magnitude, (Figure 10, right column) which, given the large 1σ ranges, may in turn suggest that the conditions under which stars form are nearly constant across the entire system. In addition, the pressure of the warm component is higher than that of the cold component, which is likely attributable to the increased temperature.

Finally, the beam-averaged column density for both the warm and cold components are well constrained across the entire region, with the beam-averaged column density of the warm component varying only by about an order of magnitude from pixel to pixel (Figure 10, bottom row). Furthermore, the beam-averaged column density of the warm component is two to three orders of magnitude less than that of the cold component. Assuming a CO abundance of $x_{\rm CO} = 3 \times 10^{-4}$ (Kamenetzky et al. 2012), the total mass of the warm component across the entire map ($\log(M_{\rm warm}/M_\odot) = 6.2^{+0.2}_{-0.2}$) is only ~0.1% that of the cold component ($\log(M_{\rm cold}/M_\odot) = 9.1^{+0.3}_{-0.9}$).

3.3.2. CO and [C I]

We expand upon our likelihood analysis by assuming both [C I] transitions trace the same molecular gas as CO. Ikeda et al. (2002) found that in the Orion GMC, [C I] $^3P_1$–$^3P_0$ and ^{13}CO $J = 1$–0 show structural similarities across the entire cloud both spatially and in velocity, suggesting that both transitions trace much of the same molecular gas, especially in the denser

regions of GMCs. Furthermore, our ratio of the two [C I] transitions, along with the CO-only molecular gas temperature, strongly suggests that it originates from cold, rather than warm, molecular gas (Section 3.1).

We fit all of the pixels in our maps where we have a detection in all of the CO and both [C I] transitions with both a cold and warm component following the same procedure in Section 3.3.1 with the following addition. We include the [C I] emission in the cold component only and not the warm component, assuming it does not contribute appreciably to the molecular gas traced by the higher J CO transitions. We report the χ^2 goodness-of-fit parameters for both the CO and [C I] measured and calculated SLEDs separately in Table 4. It is important to note that the CO SLED is calculated from the 4DMax solutions, while the [C I] solutions are calculated from the 1DMax solutions, as only the 1DMax is calculated for the [C I] abundance relative to CO. The best-fit solution to CO for NGC 4038 and the overlap region is the $J_{\rm break} = 4$ solution, while in NGC 4039, the $J_{\rm break} = 3$ solution presents the best solution. Furthermore, the best-fit solution for [C I] in all three regions is the $J_{\rm break} = 4$ solution. Therefore, we report the $J_{\rm break} = 4$ solution for consistency with our CO-only results.

The measured and calculated CO and [C I] SLEDs are shown in Figure 7, while the optical depths are shown in Figure 8. The behavior of the cold and warm components of the best-fit SLED
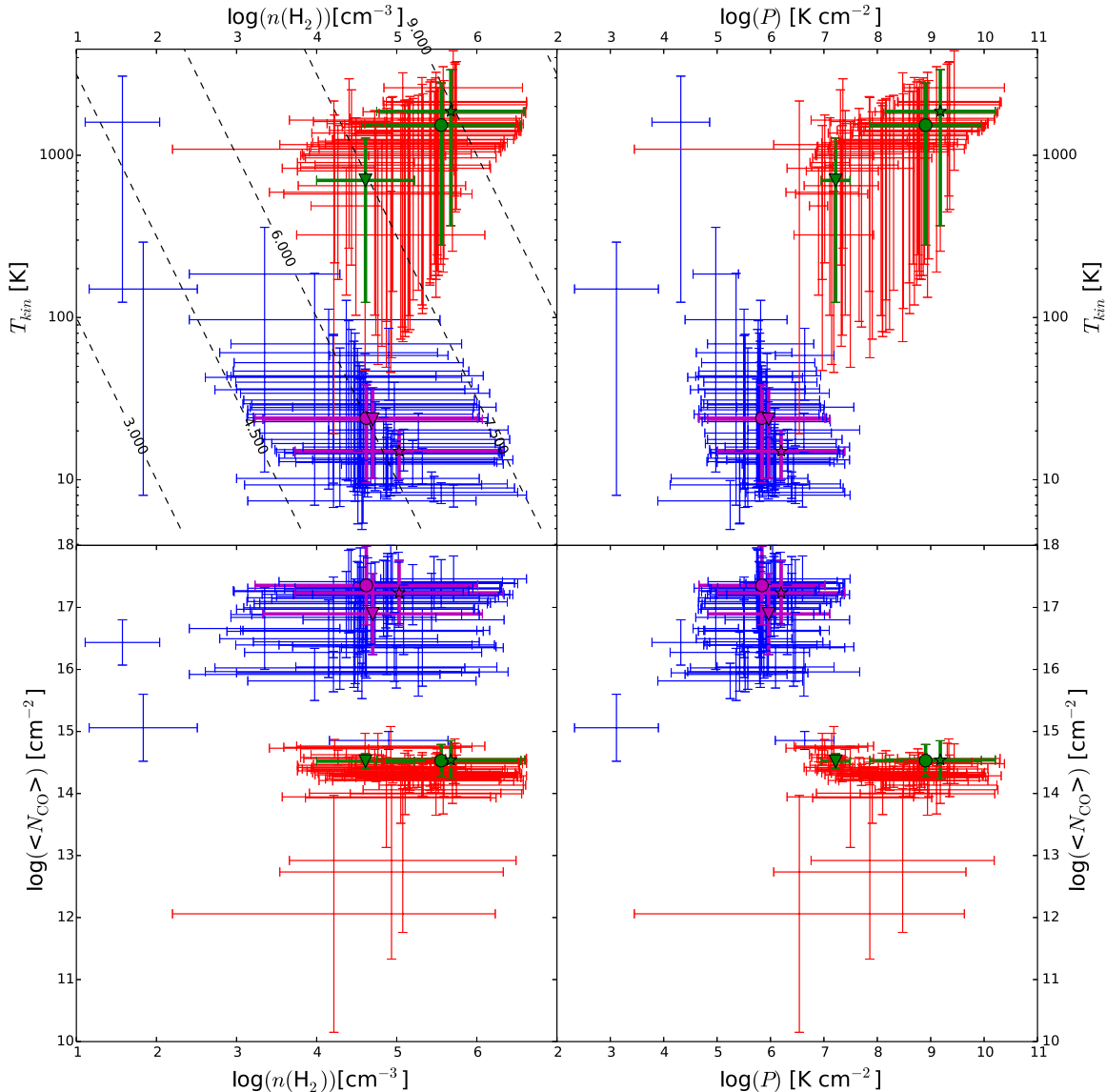
Figure 10. CO-only, non-LTE radiative transfer results for every pixel in our maps for which we detect all eight CO and both [C I] transitions. The temperature (top row) and beam-averaged column density (bottom row) are compared with the molecular gas density (left column) and pressure (right column) for both the cold (blue) and warm (red) components. The error bars correspond to the 1σ range for each physical parameter. The results for NGC 4038 (star), the overlap region (circle), and NGC 4039 (triangle) are indicated by the thick magenta (cold) and green (warm) symbols and lines. Note the location where the vertical and horizontal error bars cross corresponds to the midpoint of the 1σ range and not the most probable value. The dashed diagonal lines in the top-left plot correspond to contours of constant pressure.

(A color version of this figure is available in the online journal.)

for all three regions is strikingly similar to the CO-only results. Furthermore, in all three regions, the measured [C I] flux is reproduced. Once again, the warm component is more optically thin than the cold component (Figure 8). In addition, the [C I] emission is optically thin, as assumed in our [C I] LTE analysis. As in the CO-only solutions, when [C I] is included both a cold ($\lesssim 30$ K) and a warm ($\gtrsim 200$ K) component are recovered (Tables 7 and 8). However, in the CO and [C I] solution, the density of the cold component in all three components is better constrained than in the CO-only solution (Figure 11), along with the density of the warm component in the overlap region and NGC 4039.

For the remaining pixels in the map, the addition of [C I] to the radiative transfer analysis does not change the resulting 1σ ranges for the various physical parameters (Figure 12). As in the CO solution, we find both a warm and cold component

with comparable densities. The beam-averaged column density of the warm component is less than in the cold component. The pressure of the warm component is once again higher than in the cold component, while remaining nearly constant for each component separately. Furthermore, we find that the mass of the warm component ($\log(M_{\mathrm{warm}}/M_{\odot}) = 6.2^{+0.3}_{-0.2}$) is only $\sim 0.2\%$ that of the cold component ($\log(M_{\mathrm{cold}}/M_{\odot}) = 8.9^{+0.3}_{-0.7}$).

3.4. Molecular Gas Mass Correction

The total molecular gas mass calculated from our radiative transfer modeling will be slightly smaller than the true molecular gas mass, as we only modeled the CO and [C I] emission in pixels where we detect both [C I] and all eight CO transitions. We can estimate the missing mass using the CO $J = 3$–2 map as it encompasses the entire CO emitting region in the Antennae. The total integrated intensity in the CO $J = 3$–2 map

Table 7
Cold Component Likelihood Results: CO and [C I]

Source	Parameter	Median	1σ Range	1D Max	4D Max	Unit
NGC 4038	$T_{\rm kin}$	24	18–33	25	25	(K)
	$n(H_2)$	$10^{3.66}$	$10^{3.08}$–$10^{4.26}$	$10^{3.74}$	$10^{3.57}$	(cm^{-3})
	$N_{\rm CO}$	$10^{19.12}$	$10^{18.58}$–$10^{19.62}$	$10^{19.40}$	$10^{19.40}$	(cm^{-2})
	Φ_A	$10^{-2.09}$	$10^{-2.21}$–$10^{-1.96}$	$10^{-2.07}$	$10^{-2.07}$	
	P	$10^{5.03}$	$10^{4.51}$–$10^{5.57}$	$10^{5.22}$	$10^{5.22}$	(K cm^{-2})
	$\langle N_{\rm CO}\rangle$	$10^{17.09}$	$10^{16.58}$–$10^{17.58}$	$10^{17.62}$	$10^{17.62}$	(cm^{-2})
	$X_{\rm [C I]}/X_{\rm CO}$	$10^{-0.65}$	$10^{-1.11}$–$10^{-0.16}$	$10^{-0.95}$	$10^{-0.95}$	
	$N_{\rm [C I]}$	$10^{18.50}$	$10^{18.34}$–$10^{18.71}$	$10^{18.65}$	$10^{18.65}$	
Overlap region	$T_{\rm kin}$	20	15–27	21	21	(K)
	$n(H_2)$	$10^{3.67}$	$10^{2.90}$–$10^{4.42}$	$10^{4.00}$	$10^{3.91}$	(cm^{-3})
	$N_{\rm CO}$	$10^{19.13}$	$10^{18.44}$–$10^{19.69}$	$10^{19.59}$	$10^{18.84}$	(cm^{-2})
	Φ_A	$10^{-1.83}$	$10^{-1.96}$–$10^{-1.66}$	$10^{-1.86}$	$10^{-1.79}$	
	P	$10^{4.91}$	$10^{4.28}$–$10^{5.61}$	$10^{4.32}$	$10^{4.32}$	(K cm^{-2})
	$\langle N_{\rm CO}\rangle$	$10^{17.38}$	$10^{16.76}$–$10^{17.87}$	$10^{17.59}$	$10^{17.59}$	(cm^{-2})
	$X_{\rm [C I]}/X_{\rm CO}$	$10^{-0.49}$	$10^{-0.98}$–$10^{0.10}$	$10^{-0.74}$	$10^{-0.74}$	
	$N_{\rm [C I]}$	$10^{18.65}$	$10^{18.47}$–$10^{18.86}$	$10^{18.77}$	$10^{18.77}$	
NGC 4039	$T_{\rm kin}$	21	16–28	21	21	(K)
	$n(H_2)$	$10^{3.79}$	$10^{3.07}$–$10^{4.44}$	$10^{4.00}$	$10^{4.00}$	(cm^{-3})
	$N_{\rm CO}$	$10^{19.01}$	$10^{18.38}$–$10^{19.65}$	$10^{19.65}$	$10^{18.83}$	(cm^{-2})
	Φ_A	$10^{-2.21}$	$10^{-2.36}$–$10^{-2.03}$	$10^{-2.21}$	$10^{-2.14}$	
	P	$10^{5.09}$	$10^{4.45}$–$10^{5.66}$	$10^{5.34}$	$10^{5.34}$	(K cm^{-2})
	$\langle N_{\rm CO}\rangle$	$10^{16.86}$	$10^{16.33}$–$10^{17.44}$	$10^{16.49}$	$10^{16.49}$	(cm^{-2})
	$X_{\rm [C I]}/X_{\rm CO}$	$10^{-0.17}$	$10^{-0.72}$–$10^{0.36}$	$10^{-0.53}$	$10^{-0.53}$	
	$N_{\rm [C I]}$	$10^{18.87}$	$10^{18.63}$–$10^{19.10}$	$10^{19.03}$	$10^{19.03}$	

Table 8
Warm Component Likelihood Results: CO and [C I]

Source	Parameter	Median	1σ Range	1D Max	4D Max	Unit
NGC 4038	$T_{\rm kin}$	1065	347–3397	647	3999	(K)
	$n(H_2)$	$10^{5.75}$	$10^{4.77}$–$10^{6.61}$	$10^{7.00}$	$10^{4.26}$	(cm^{-3})
	$N_{\rm CO}$	$10^{17.04}$	$10^{15.29}$–$10^{18.83}$	$10^{16.10}$	$10^{14.68}$	(cm^{-2})
	Φ_A	$10^{-2.57}$	$10^{-4.30}$–$10^{-0.81}$	$10^{-4.57}$	$10^{-0.36}$	
	P	$10^{9.29}$	$10^{8.17}$–$10^{10.23}$	$10^{9.44}$	$10^{9.44}$	(K cm^{-2})
	$\langle N_{\rm CO}\rangle$	$10^{14.45}$	$10^{14.19}$–$10^{14.83}$	$10^{14.29}$	$10^{14.29}$	(cm^{-2})
Overlap region	$T_{\rm kin}$	1425	430–3811	2666	4425	(K)
	$n(H_2)$	$10^{4.23}$	$10^{4.00}$–$10^{4.73}$	$10^{4.09}$	$10^{4.00}$	(cm^{-3})
	$N_{\rm CO}$	$10^{16.39}$	$10^{15.12}$–$10^{17.80}$	$10^{14.80}$	$10^{14.95}$	(cm^{-2})
	Φ_A	$10^{-1.86}$	$10^{-3.25}$–$10^{-0.58}$	$10^{-0.14}$	$10^{-0.29}$	
	P	$10^{7.45}$	$10^{7.26}$–$10^{7.73}$	$10^{7.39}$	$10^{7.39}$	(K cm^{-2})
	$\langle N_{\rm CO}\rangle$	$10^{14.55}$	$10^{14.40}$–$10^{14.70}$	$10^{14.55}$	$10^{14.55}$	(cm^{-2})
NGC 4039	$T_{\rm kin}$	629	203–2390	431	431	(K)
	$n(H_2)$	$10^{4.35}$	$10^{3.97}$–$10^{5.00}$	$10^{3.91}$	$10^{4.51}$	(cm^{-3})
	$N_{\rm CO}$	$10^{16.30}$	$10^{14.99}$–$10^{17.73}$	$10^{14.78}$	$10^{15.15}$	(cm^{-2})
	Φ_A	$10^{-1.91}$	$10^{-3.33}$–$10^{-0.59}$	$10^{-0.14}$	$10^{-0.64}$	
	P	$10^{7.27}$	$10^{7.09}$–$10^{7.57}$	$10^{7.26}$	$10^{7.26}$	(K cm^{-2})
	$\langle N_{\rm CO}\rangle$	$10^{14.42}$	$10^{14.28}$–$10^{14.51}$	$10^{14.47}$	$10^{14.47}$	(cm^{-2})

is 724 K km s^{-1}, while the integrated intensity of the pixels used in RADEX modeling is 563 K km s^{-1}, corresponding to only $\sim$78% of the total integrated intensity. Therefore, we apply a correction of $\sim$22% to the total molecular gas masses calculated in Sections 3.3.1 and 3.3.2.

In addition, the CO $J = 1$–0 map does not extend far beyond the bright CO-emitting regions in the Antennae, suggesting that there could be missing flux from beyond the edges of the map. Using the CO $J = 3$–2 map, we estimate that only $\sim$88% of the total integrated intensity is within the bounds of the CO $J = 1$–0 map. We correct for this missing flux when calculating the total cold molecular gas mass from the CO $J = 1$–0 map in Section 4.

4. DISCUSSION

4.1. Radiative Transfer Modeling Results

4.1.1. Comparison with Previous Results

Both Zhu et al. (2003) and Bayet et al. (2006) previously performed a radiative transfer analysis using ground-based CO data. Bayet et al. (2006) used the ratios of (^{12}CO $J = 3$–2)/(^{12}CO $J = 6$–5), (^{12}CO $J = 2$–1)/(^{12}CO $J = 6$–5), and (^{12}CO $J = 3$–2)/(^{13}CO $J = 3$–2) to fit a single warm component in the nucleus of NGC 4038 and the overlap region. The primary difference between their model for a warm component and ours is that we consider the contributions of the cold
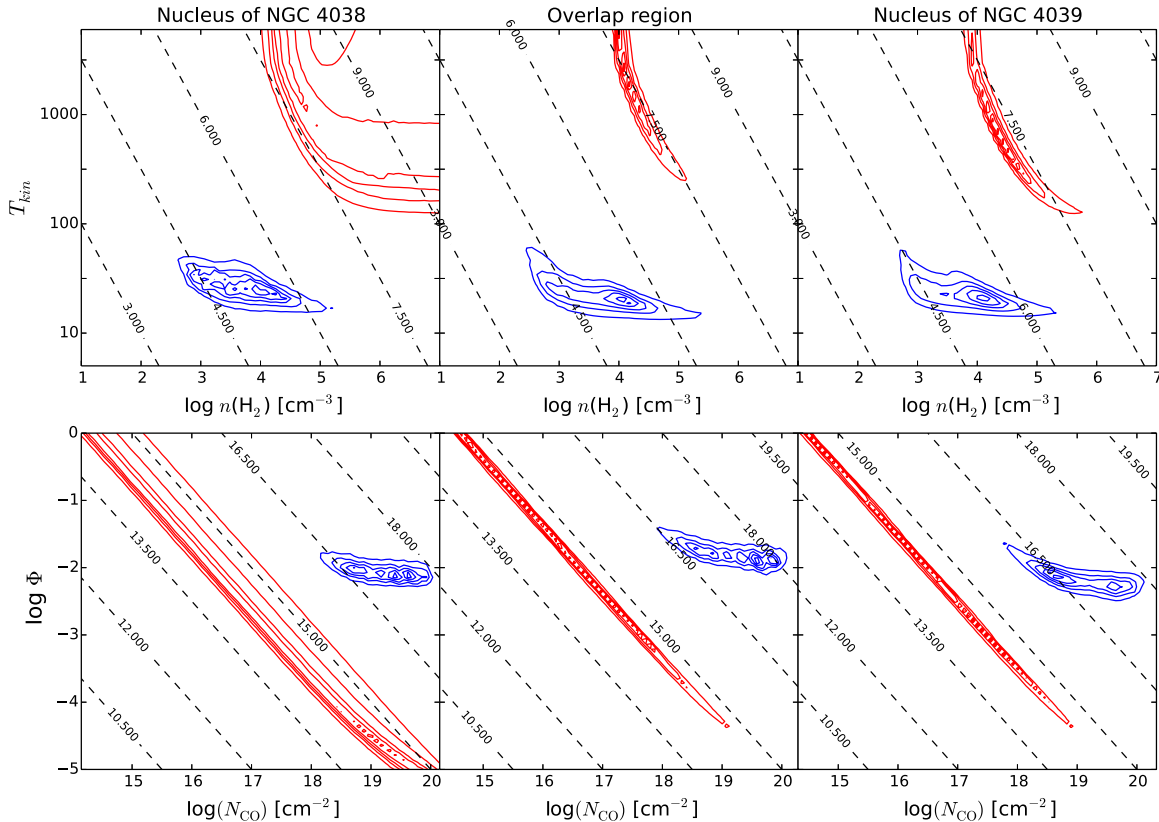
Figure 11. Same as Figure 9, except for the solutions including both CO and [C I].
(A color version of this figure is available in the online journal.)

component to the lower J CO transitions while they do not. They found that the temperature and density vary significantly between NGC 4038 and the overlap region. In NGC 4038, the temperature that their model predicts ($T_{\rm kin} = 40$ K) does not fall within either the cold or warm component 1σ range for either the CO or the CO and [C I] solutions, while the density ($n({\rm H_2}) = 3.5 \times 10^5$ cm^{-2}) agrees within 1σ of the CO-only cold component and both the CO-only and the CO and [C I] warm components. In the overlap region, their model temperature (145 K) does not fall within any of our temperature ranges, while their density ($n({\rm H_2}) = 8.0 \times 10^3$ cm^{-2}) agrees with both of our cold-component densities. Furthermore, their models predict that the ^{12}CO SLED peaks at the $J = 3$–2 transition, while our observations indicate that it instead peaks at the $J = 1$–0 transition (Figure 7). In our models, we find that the warm component only contributes significantly to the $J = 6$–5, $J = 7$–6, and $J = 8$–7 transitions (Figure 7), suggesting that Bayet et al. (2006) is, at least in part, modeling a cold component of the molecular gas.

In comparison, using various ratios of the ^{12}CO $J = 1$–0 to $J = 3$–2 and the isotopologue ^{13}CO $J = 2$–1 and $J = 3$–2 transitions, Zhu et al. (2003) fit both a single and a two-component model in NGC 4038, NGC 4039, and the overlap region. The results from the single-component fit suggest that these transitions are tracing a cold component ($T_{\rm kin} \sim 20$–40 K) with density $n({\rm H_2}) \sim 10^3$–10^4 cm^{-3}, both comparable to our cold component. This agreement is unsurprising, as our models suggest that, in all three regions, the cold component dominates the emission from the ^{12}CO $J = 1$–0 to $J = 3$–2 transitions. For the two-component fit, Zhu et al. (2003) argue that there must be a low-density component ($n({\rm H_2}) \sim 10^3$ cm^{-3}) that

dominates the optically thick ^{12}CO emission and a high-density component ($n({\rm H_2}) \sim 10^5$ cm^{-3}) that dominates the optically thin ^{13}CO emission. As a result, they find two temperature components, a cold component ($T_{\rm kin} = 36$–120 K) and a warm component ($T_{\rm kin} = 42$–220 K), with the density and temperature of the two components depending upon the ratio of ^{12}CO/^{13}CO, which varies from 40 to 70. In our case, the warm component dominates the high J CO transitions, which are optically thin, while the cold component dominates the optically thick lower J CO transitions (Figure 8). Furthermore, while the density is not well constrained, our results suggest that the cold component has a lower density than the warm component, indicating that our lower density component does coincide with the optically thick transitions, as found by Zhu et al. (2003).

4.1.2. Comparison Across the Antennae

Both the LTE and non-LTE radiative transfer analyses suggest there is cold molecular gas across the Antennae with both sets of calculated temperatures agreeing within the uncertainties (Figure 6). Furthermore, the non-LTE analysis suggests that warm molecular gas ($T_{\rm kin} \gtrsim 100$ K) is prevalent throughout the system; however, the warm component temperature is poorly constrained (Figures 10 and 12). Both sets of RADEX solutions for the cold molecular gas suggest that the molecular gas has a similar temperature (~ 20 K) and density ($\sim 10^3$–10^4 cm^{-3}) in all three regions. Similarly, the densities of the warm component in the overlap region and NGC 4039 are similar ($\sim 10^{4.5}$ cm^{-3}), while it is higher in NGC 4038 ($\gtrsim 10^{4.75}$ cm^{-3}). In addition, the CO and [C I] RADEX solution suggests that the density of the warm component is slightly higher than that of the cold component; however, for the overlap region and NGC 4039, the
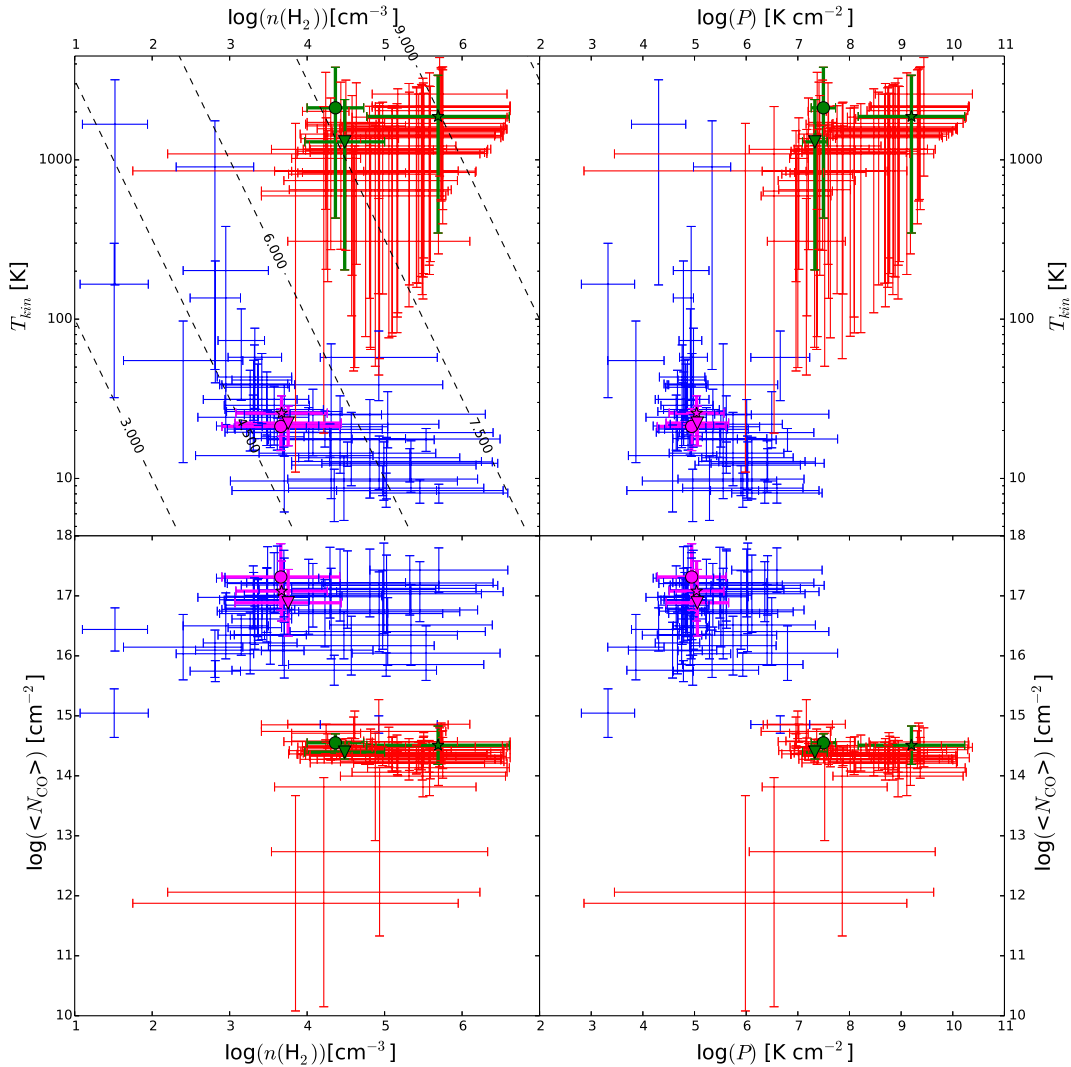
Figure 12. Same as Figure 10, except for solutions including both CO and [C I].
(A color version of this figure is available in the online journal.)

1σ ranges of the densities of the cold and warm components overlap and so no firm conclusions can be drawn concerning these densities.

Brandl et al. (2009) calculated the temperature of the warm molecular gas from Infrared Spectrograph *Spitzer* observations of the H_2 S(1) and S(2) transitions and found a warm gas temperature of 270–370 K in both nuclei and at numerous locations in the overlap region. This temperature range falls within our warm component 1σ ranges for these three regions. This suggests that H_2 is tracing the same warm gas as the upper J CO transitions.

The pressure across the Antennae in each of the cold and warm components is nearly constant within the uncertainties (Figures 10 and 12), while the pressure in the warm component is $\sim$2–3 orders of magnitude larger than that in the cold component. The temperature is only $\sim$1–3 orders of magnitude larger in the warm component over the cold component and may be sufficient to explain the increased pressure.

4.2. CO Abundance and the CO-to-H_2 Conversion Factor

For the purpose of our RADEX modeling, we assumed a CO abundance of $x_{CO} = 3 \times 10^{-4}$ (Kamenetzky et al. 2012). Using this abundance, we recover a corrected cold gas

mass of $M_{cold} = 1.5^{+1.7}_{-1.3} \times 10^9$ $M_\odot$, which would correspond to a CO $J = 1$–0 luminosity-to-mass conversion factor of $\alpha_{CO} \sim 0.7$ $M_\odot$ pc^{-2} $(K\,km\,s^{-1})^{-1}$. This value is lower than the value for the Milky Way, but agrees with the value of $\alpha_{CO} = 0.8$ $M_\odot$ pc^{-2} $(K\,km\,s^{-1})^{-1}$ from Downes & Solomon (1998), which is the value typically assumed for ULIRGs. Arp 299, another relatively nearby merger ($D_L = 46\,Mpc$), is brighter in the IR than the Antennae ($L_{IR} \sim 7 \times 10^{11}$ $L_\odot$). Sliwa et al. (2012) found that for a CO abundance of 3×10^{-4}, $\alpha_{CO} = 0.4$ $M_\odot$ pc^{-2} $(K\,km\,s^{-1})^{-1}$, which agrees with the value calculated for LIRGs ($\alpha_{CO} \sim 0.6 \pm 0.2$ $M_\odot$ pc^{-2} $(K\,km\,s^{-1})^{-1}$; Papadopoulos et al. 2012).

However, the true CO abundance in the Antennae may be smaller (Zhu et al. 2003). We investigate the CO abundance by comparing the total warm molecular gas mass we calculate in the Antennae with values from previous studies. Brandl et al. (2009) measured the total warm ($\sim$300 K) gas mass in the Antennae using *Spitzer* observations of the H_2 S(1), S(2), and S(3) transitions to be 2.5×10^7 $M_\odot$. Our corrected warm-component ($\gtrsim$100 K) mass from the CO-only RADEX solution is $2.2^{+1.3}_{-1.0} \times 10^6$ $M_\odot$, while for the CO and [C I] solution it is $2.2^{+1.5}_{-1.0} \times 10^6$ $M_\odot$. Both of our calculated masses are a factor of $\sim$10 less than the Brandl et al. (2009) mass. Assuming our

warm gas solution is tracing the same gas as the H_2 lines, a CO abundance of $x_{CO} = 3 \pm 2 \times 10^{-5}$ is required to recover this warm gas mass. This abundance ratio falls in the range of $\sim 10^{-5}$–10^{-4}, which is typically assumed for starburst galaxies (Zhu et al. 2003; Mao et al. 2000).

Using this abundance ratio of 3×10^{-5}, we obtain a cold molecular gas mass for the CO-only solution of $M_{cold} = 1.5^{+1.7}_{-1.3} \times 10^{10} \ M_\odot$. In order to recover the same mass from our CO $J = 1$–0 map, we would require a CO $J = 1$–0 luminosity-to-mass conversion factor of $\alpha_{CO} \sim 7 \ M_\odot \ pc^{-2} \ (K \ km \ s^{-1})^{-1}$. This is consistent with the Milky Way value ($\alpha_{CO} \sim 4$–$9 \ M_\odot \ pc^{-2} \ (K \ km \ s^{-1})^{-1}$) and the value for M31, M33, and the Large Magellanic Cloud ($\alpha_{CO} \sim 3$–$9 \ M_\odot \ pc^{-2} \ (K \ km \ s^{-1})^{-1}$; Leroy et al. 2011). Wilson et al. (2003) calculated the CO-to-H_2 conversion factor in the Antennae by comparing the virial mass of resolved SGMCs to the integrated intensity. They found that the conversion factor in the Antennae agrees with the value for the Milky Way ($\alpha_{CO} \sim 6.5 \ M_\odot \ pc^{-2} \ (K \ km \ s^{-1})^{-1}$). As such, we adopt a value of $\alpha_{CO} \sim 7 \ M_\odot \ pc^{-2} \ (K \ km \ s^{-1})^{-1}$ and $x_{CO} \sim 3 \times 10^{-5}$ for the CO-to-H_2 conversion factor and the CO abundance, respectively.

4.3. Heating and Cooling of the Molecular Gas

In this section, we discuss the possible heating and cooling mechanisms for the molecular gas in the Antennae.

4.3.1. Cooling

CO, [O I] 63 μm, [C II], and H_2 will all contribute to the overall cooling budget of both the cold and warm molecular gas; however, which coolant dominates is dependent on the overall state of the molecular gas. In particularly warm molecular gas ($T_{kin} \gtrsim 1000$ K), H_2 will be the dominant coolant (e.g., Arp 220; Rangwala et al. 2011) while for cooler gas, [C II], [O I] 63 μm, and CO will also contribute to the total cooling of molecular gas. We investigate the possible cooling mechanisms in order to determine the total rate of cooling of molecular gas in the Antennae.

H_2 cooling only becomes important in molecular gas where the temperature is $T_{kin} > 100$ K. Le Bourlot et al. (1999) calculated curves for the total H_2 cooling per unit mass, which is dependent upon the molecular gas density ($n(H_2)$), the kinetic temperature T_{kin}, the H/H_2 ratio, and the ratio of ortho-to-para H_2, all of which are input parameters for the calculated cooling curves. Le Bourlot et al. (1999) have provided a program that interpolates their cooling curves for a given set of input parameters, allowing us to estimate the H_2 cooling for each pixel in the Antennae using the RADEX-calculated $n(H_2)$ and T_{kin} from the warm component, along with the mass of the warm molecular gas. We assume that $H/H_2 = 0.01$ and that the ratio of ortho-to-para is 1. It is important to note that changing the ortho-to-para ratio to 3 does not change the total H_2 cooling significantly (Le Bourlot et al. 1999). The H_2 cooling is highly dependent on the kinetic temperature and, given that the temperature of our warm component is not particularly well constrained, we opt to use the 1σ lower bound on the temperature in each pixel to calculate a lower limit to the H_2 cooling. There is only a $\sim 10\%$–15% difference between the cooling rate calculated when using either the 1σ lower bound or the most probable value for the molecular gas density. We opt to use the most probable value as it likely represents a more realistic density (i.e., see Figures 9 and 11).

We assume a CO abundance of 3×10^{-5}, as determined in Section 4.2, and apply the same pixel incompleteness correction as we did for the mass. We calculate the total H_2 cooling to be $\sim 4.9 \times 10^7 \ L_\odot$ from the CO-only RADEX results and $\sim 6.5 \times 10^7 \ L_\odot$ from the CO and [C I] RADEX results. Brandl et al. (2009) measured a luminosity of $9.2 \times 10^6 \ L_\odot$ for the H_2 S(3) transition. Given that the luminosity of the S(2) and S(1) transitions are comparable to the S(3) transition (Brandl et al. 2009), our calculated H_2 cooling is reasonably consistent with this measurement.

Next, we estimate the total cooling contribution from CO (L_{CO}) by summing the total luminosity for all of our CO transitions. Each individual transition contributes between 1% and 25% of the total CO cooling, with the $J = 1$–0 transition contributing only 1% and the $J = 4$–3 and $J = 6$–5 transitions contributing $>20\%$. The remaining five transitions each contribute between 6% and 14% to the total CO cooling. In addition, we apply the same pixel incompleteness correction as before and we calculate the contribution of CO to the overall cooling to be $L_{CO} = 1.8 \times 10^7 \ L_\odot$.

In order to calculate the total contribution from [C II] to the total cooling budget, we must correct for the fraction of emission that arises from ionized gas. The ratio of [C II] to the [N II] transition at 1461 GHz ($L_{[C II]}/L_{[N II]}$) provides a useful diagnostic for determining the contribution from ionized gas (Oberst et al. 2006), as emission from [N II] arises entirely from ionized gas (Malhotra et al. 2001). This ratio depends upon the ionized gas density, n_e, with the ratio varying from ~ 2.4 to ~ 4.3 (Oberst et al. 2006), assuming solar abundances for C^+ and N^+. We assume $L_{[C II]}/L_{[N II]} \sim 3.5$ for the ionized gas as it is near the midpoint between the two extremes for the ratio and correct the [C II] emission by assuming any excess in $L_{[C II]}$ cools the molecular gas. This value is an upper limit as some of the [C II] emission will originate from atomic gas.

We calculate the ratio of $L_{[C II]}/L_{[N II]}$ by first convolving our [C II] map to the beam of the [N II] map. We approximate the SSW beam at 1461 GHz as a $17''$ Gaussian and use the kernels from Aniano et al. (2011). We then align our [C II] map to the $3''$ pixel scale [N II] map and calculate the ratio of $L_{[C II]}/L_{[N II]}$. We linearly interpolate any pixels in which we do not have measurements for [N II], due to the large beam size. We correct each pixel in our [C II] map before summing over the entire map. After this correction, we calculate that the contribution to the total molecular gas cooling from [C II] to be $L_{[C II]} = 5.5 \times 10^7 \ L_\odot$. In comparison, without the correction for [C II] from ionized gas, the total [C II] luminosity is $L_{[C II]} = 9.4 \times 10^7 \ L_\odot$ from the PACS observations.

The total [C II] luminosity corresponds to only $\sim 23\%$ of the total [C II] luminosity calculated by Nikola et al. (1998) using observations from the Kuiper Airborne Observatory (KAO). Their map, however, covered a region of $5' \times 5'$, which is significantly larger than the region mapped by PACS. Furthermore, Nikola et al. (1998) compared their KAO observations with those from the *ISO* and found that the KAO flux is a factor of two larger across the same region. The KAO observations also have a calibration uncertainty of 30%. Given the large uncertainties in these previous observations, we elect to estimate the total [C II] flux from the PACS observations. We estimate the missing flux in our [C II] flux by comparing the total PACS 160 μm flux with the PACS 160 μm flux in the region mapped in our [C II] observation. The PACS 160 μm was graciously provided by Klaas et al. (2010) and covers a total region of approximately 8.5×9.5 centered on the Antennae. We estimate that only $\sim 70\%$

of the total [C II] luminosity is in our PACS map, which gives us an ionized-gas-corrected luminosity of $L_{\rm [C\,II]} = 7.9 \times 10^7 \, L_\odot$. Due to the uncertainty in the KAO flux, we use this corrected luminosity for the contribution of [C II] to the total cooling budget.

We also calculate the total cooling due to [O I] 63 μm to be $L_{\rm [O\,I]63} = 3.6 \times 10^7 \, L_\odot$ from the PACS observations. The ratio of $L_{\rm [C\,II]}/L_{\rm [O\,I]63}$ is not constant, typically increasing further away from the nuclear regions of galaxies, as [C II] starts to dominate the cooling in more diffuse environments. As such, we do not correct the [O I] 63 μm emission for missing flux when including it in our total cooling budget. We estimate the total cooling budget for the molecular gas in the Antennae to be $\sim 2.0 \times 10^8 \, L_\odot$. Assuming a molecular gas mass of $1.5 \times 10^{10} \, M_\odot$ (see Section 4.2), this would correspond to $\sim 0.01 \, L_\odot/M_\odot$, with [C II] dominating the cooling, followed by H$_2$, [O I] 63, and CO. In comparison, the cooling per unit mass in M82 and Arp220 is $\sim 3 \, L_\odot/M_\odot$ and $\sim 20 \, L_\odot/M_\odot$, respectively (see Section 4.4).

4.3.2. Mechanical Heating

We consider two forms of mechanical heating: turbulent heating (Bradford et al. 2005) and supernova and stellar wind heating (Maloney 1999). Turbulent heating is caused by the turbulent motion of the molecular gas, which can be caused by a strong interaction or ongoing merger. We can calculate the energy per unit mass injected back into the Antennae using (Bradford et al. 2005):

$$\frac{L}{M} = 1.10 \left(\frac{v_{\rm rms}}{25 \, {\rm km \, s^{-1}}} \right)^3 \left(\frac{1 \, {\rm pc}}{\Lambda_d} \right) \frac{L_\odot}{M_\odot}, \qquad (6)$$

where $v_{\rm rms}$ is the turbulent velocity and Λ_d is the size scale. We assume the turbulent heating rate is equal to our calculated cooling rate ($L/M \sim 0.01 \, L_\odot/M_\odot$) and, for a size scale of $\Lambda_d = 1$ pc, we calculate a turbulent velocity of $v_{\rm rms} \sim 5 \, {\rm km \, s^{-1}}$. For a size scale of $\Lambda_d = 1000$ pc, the corresponding turbulent velocity is $v_{\rm rms} \sim 52 \, {\rm km \, s^{-1}}$. The line widths for the resolved SGMCs from Wilson et al. (2003) are on the order of 10–50 km s^{-1}, which correspond to turbulent velocities on the order of $v_{\rm rms} \sim 5$–25 km s^{-1} on a size scale of 1 kpc. This is comparable to the values calculated for a 1 pc size scale, which is on the order of the Jeans length for our warm component. Furthermore, it is comparable to velocities from simulations of extreme star-forming galaxies ($\sim$30–140 km s^{-1}; Downes & Solomon 1998). Given that the Antennae is both undergoing an intense starburst (Hibbard 1997) and is in the process of merging, a turbulent velocity of ~ 5 km s^{-1} is not unreasonable. Thus, turbulent velocity is a possible contributor to heating in the Antennae.

The mechanical energy due to supernovae is (Maloney 1999)

$$L_{\rm SN} \sim 3 \times 10^{43} \left(\frac{\nu_{\rm SN}}{1 \, {\rm yr^{-1}}} \right) \left(\frac{E_{\rm SN}}{10^{51} \, {\rm erg}} \right) {\rm erg \, s^{-1}}, \qquad (7)$$

where $\nu_{\rm SN}$ is the supernova rate and $E_{\rm SN}$ is the energy released per supernova ($\sim 10^{51}$ erg). In the Antennae, the observed global supernova rate is $\nu_{\rm SN} \sim 0.2$–0.3 yr^{-1} (Neff & Ulvestad 2000). This corresponds to a rate of $L_{\rm SN} \sim (1.6$–2.3$) \times 10^9 \, L_\odot$ for the energy released from supernova. If we assume that the contribution from stellar winds is comparable (Rangwala et al. 2011), the total mechanical energy injected into the interstellar medium (ISM) from supernovae and stellar winds is $(3.2$–4.6$) \times 10^9 \, L_\odot$. Only $\sim 5\%$ of this energy would be required

to balance the measured cooling rate of $\sim 2.0 \times 10^8 \, L_\odot$. This situation corresponds to a supernova heating efficiency of 0.05. In comparison, in the Milky Way only $\sim 10\%$ of the total energy from supernovae is injected back into the surrounding ISM in the form of kinetic energy, which in turn contributes to both moving and heating the gas (Thornton et al. 1998).

By comparing the position of the nonthermal radio sources in Neff & Ulvestad (2000), along with their respective derived supernova rates, with the beams in Figure 1, we estimate that 14%, 6%, and 66% of the supernova originate from NGC 4038, NGC 4039, and the overlap region, respectively. In comparison, we estimate that 9%, 15%, and 54% of the [C II] emission (corrected for the ionized gas fraction), which is the dominant coolant (see Section 4.3.1), originates from NGC 4038, NGC 4039, and the overlap region, respectively. The differences between the relative heating and cooling rates could be an indicator of a different balance among the varying sources of heating in the three regions.

Globally, supernovae and stellar winds are a possible source of heating in the Antennae. Given the turbulent nature of the molecular gas as a result of the ongoing merger, it is likely that both the merger-induced turbulent motion as well as supernovae and stellar winds contribute to the heating, with their relative importance dependent on the local environment within the Antennae.

4.3.3. Photon-dominated Regions

PDRs are neutral regions located near the surfaces of molecular clouds that are irradiated by strong far-ultraviolet (FUV) radiation (Tielens & Hollenbach 1985). The FUV photons are absorbed by dust grains and may liberate electrons through the photoelectric effect; the liberated electrons in turn heat the gas. The strength of the incident FUV field, G_0, is measured in units of the Habing interstellar radiation field, which is 1.3×10^{-4} erg cm^{-2} s^{-1} sr^{-1} (Wolfire et al. 2010) and is the strength of the local interstellar field. This FUV radiation will photodissociate the CO located near the edge of the molecular cloud where the FUV radiation is the strongest. Typically, massive, young, hot stars are the source of the FUV radiation and as such can have a profound effect on the chemical and physical state of the entire molecular cloud.

We use PDR models (Hollenbach et al. 2012; M. Wolfire 2012, private communication) to interpret the observed CO SLED for the three regions in the Antennae (Table 1). These models consist of a grid of CO fluxes for transitions from $J = 1$–0 to $J = 29$–28 spanning a large range of densities ($n({\rm H_2}) = 10^{1.0}$–$10^{7.0}$ cm^{-3}) and incident FUV fluxes ($G_0 = 10^{-0.5}$–$10^{6.5}$). Furthermore, these models typically assume that the FIR flux is a factor of two larger than the incident FUV flux. Using these models, along with the densities calculated from our radiative transfer analysis, we can constrain the FUV field strength. In this section, we model the ratio of two CO transitions ($J = 3$–2 and $J = 6$–5) to the FIR flux, along with the ratios of numerous CO transitions to each other.

We estimate the FIR luminosity ($L_{\rm FIR}$) by first calculating the total IR luminosity ($L_{\rm TIR}$) using Equation (4) from Dale & Helou (2002). We acquired the Multiband Imaging Photometer for *Spitzer* 24 μm map from the *Spitzer* archive, while we were graciously provided with the PACS 70 μm and 160 μm photometric maps by Klaas et al. (2010). All three maps are convolved to the 160 μm beam size (12″.13; PACS Observer's

Manual version 2.4[13]) using the appropriate convolution kernels and scripts from Aniano et al. (2011).[14] Next, we assume a ratio of $L_{TIR}/L_{FIR} \sim 2$ (Dale et al. 2001) and calculate a map of L_{FIR}. This L_{FIR} map is convolved to the $43''$ beam of the FTS by first convolving it to a $15''$ Gaussian beam using the appropriate kernel from Aniano et al. (2011) and then to the $43''$ FTS beam using the same kernel used to convolve the CO $J = 3$–2 map.

We calculate the ratios of L_{CO}/L_{FIR} for the CO $J = 3$–2 transition and CO $J = 6$–5 transition for NGC 4038 (Figure 13, bottom), NGC 4039 (Figure 14, bottom), and the overlap region (Figure 15, bottom). We further constrain the field strength by plotting various ratios of CO transitions for NGC 4038 (Figure 13), NGC 4039 (Figure 14), and the overlap region (Figure 15). For all three regions, we plot the ratio of CO (3–2)/(1–0) (top left), (3–2)/(2–1) (middle left), (8–7)/(6–5) (top right), and (8–7)/(7–6) (middle right). We associate the CO $J = 3$–2 transition ratios with the cold component and $J = 6$–5 transition ratios with the warm component and as such we compare these ratios to the densities of the cold ($J = 3$–2) and warm ($J = 6$–5) components from the CO and [C I] non-LTE radiative transfer solutions. In the bottom two panels of all three figures, we combine the cold (bottom left) and warm (bottom right) CO transitions with the corresponding L_{CO}/L_{FIR} ratio.

The results for all three regions are similar: the various ratios for the warm component are consistent with a field strength of $Log(G_0) \sim 3$, while the various ratios for the cold component are consistent with a field strength of $Log(G_0) \sim 2$. It is important to note that the ratios of L_{CO}/L_{FIR} are lower limits as there will be contributions to L_{FIR} from both the cold and warm components. These lower limits correspond to upper limits in the FUV field strength G_0 (see the bottom of Figures 13, 14, and 15). We are unable to constrain the relative contributions from the warm and cold components to the total FIR luminosity and so all values for G_0 are upper limits.

Given an FUV field strength of $Log(G_0) = 3$ for our warm PDR models and assuming a ratio of $L_{FIR}/L_{FUV} \sim 2$, the corresponding FIR flux is 2.6×10^{-1} erg cm^{-2} s^{-1} sr^{-1}. The peak FIR flux, as estimated from our FIR map, in NGC 4038 is 4.9×10^{-2} erg cm^{-2} s^{-1} sr^{-1}, in NGC 4039 is 2.6×10^{-2} erg cm^{-2} s^{-1} sr^{-1}, and in the overlap region is 9.3×10^{-2} erg cm^{-2} s^{-1} sr^{-1}. In NGC 4039, the weakest of the three regions, our model PDRs would need to fill only $\sim 10\%$ of the $12''$ (~ 1.2 kpc) PACS beam in order to recover the measured peak flux. Given that the typical size scale of GMCs and stellar clusters is 10–100 pc, only a few model PDR regions are required to recover the measured FIR flux.

In comparison, our cold PDR models have an FUV field strength of $Log(G_0) = 2$, corresponding to an FIR flux of 2.6×10^{-2} erg cm^{-2} s^{-1} sr^{-1}. In NGC 4039, this would require that our model PDRs fill $\sim 100\%$ of the PACS beam. Given the face-on nature of the Antennae, coupled with previous interferometric observations of CO (e.g., Wilson et al. 2003), we do not expect PDRs to fill the $12''$ PACS beam and thus the warm PDRs must make a significant contribution to L_{FIR}. For example, if cold PDRs filled 30% of the beam and so contributed 30% of L_{FIR}, then the warm PDRs would have to account for the remaining 70% of the FIR luminosity in NGC 4039.

Bayet et al. (2006) modeled various ratios of the CO $J = 3$–2, $J = 2$–1, and $J = 6$–5 transitions, along with the ^{13}CO $J = 3$–2

transition with PDR models in NGC 4038 and the overlap region. They find an FUV field strength, in units of the Habing field, of $Log(G_0) \sim 5.4$ and a density of $n(H_2) = 3.5 \times 10^5$ cm^{-3} for the overlap region, while for NGC 4038 they find that $Log(G_0) \sim 5.6$ and $n(H_2) = 3.5 \times 10^5$ cm^{-3}. In both cases, their field strength does not lie within the fields strengths allowed by our solutions for both regions (Figures 15 and 13). Furthermore, our ratio of L_{CO}/L_{FIR} for the $J = 6$–5 transition would need to be two orders of magnitude smaller to recover such a field strength, even at very high densities (e.g., see the bottom-right panel of Figures 13 and 15). Given that our ratio provides an upper limit on G_0, we can rule out their solutions.

In comparison, Schulz et al. (2007) modeled various ratios of the peak brightness of the ^{12}CO $J = 1$–0, $J = 2$–1, and $J = 3$–2 transitions, along with the ^{13}CO $J = 1$–0 and $J = 2$–1 transitions. They apply their model to NGC 4038, NGC 4039, and the overlap region (their "interaction region"). Their findings are consistent with ours: they are able to recover their line ratios with an FUV field strength equivalent to $Log(G_0) \sim 3.2$ with densities of $n(H_2) = 10^{4.5}$, $n(H_2) = 10^{4.3}$, and $n(H_2) = 10^{4.4}$ for NGC 4038, NGC 4039, and the overlap region, respectively. All of these densities lie either within our 1σ ranges for the respective cold and warm components or lie near the boundary, further suggesting that our results are consistent with those of Schulz et al. (2007).

In summary, we model the ratios of CO $J = 3$–2 and $J = 6$–5 transitions to the FIR emission, along with various ratios of different CO transitions with PDRs. By comparing our densities as calculated from our non-LTE radiative transfer analysis, we find a field strength of $Log(G_0) \sim 3$ for PDRs in all three regions. Our field strength and densities for our PDR models are both significantly less than the values from Bayet et al. (2006), but are both consistent with the results from Schulz et al. (2007). Thus, PDRs remain as a possible source of significant heating throughout the Antennae. Further study using transitions from atomic species, such as [C II] and [O I], will be useful in further constraining not only the physical characteristics of the PDRs throughout the Antennae, but the location of these PDRs.

4.4. Comparison with Other Galaxies

The Antennae is the fourth system from the VNGS-FTS sample to be analyzed using a non-LTE radiative transfer analysis and is the only early-stage merger from our sample. Furthermore, of these four systems, it is the only one in which large-scale structure is resolved in our $43''$ beam. Of the three previously studied galaxies, the Antennae has more similarities to M82 (Kamenetzky et al. 2012) and Arp 220 (Rangwala et al. 2011). The third galaxy, NGC 1068, is a Seyfert type 2 galaxy, whose nuclear physical and chemical state is driven by an AGN (Spinoglio et al. 2012).

M82 is a nearby galaxy (3.4 Mpc) currently undergoing a starburst (Yun et al. 1993) due to a recent interaction with the nearby galaxy M81. This starburst has led to an enhanced star formation rate and as a result an IR brightness ($L_{IR} = 5.6 \times 10^{10} L_\odot$; Sanders et al. 2003) approaching that of a LIRG. Like in the Antennae, radiative transfer modeling of M82 found that there is both cold ($\lesssim 100$ K) and warm (~ 450 K) molecular gas, with the mass of the warm component ($\sim 1.5 \times 10^6 M_\odot$) being on the order of $\sim 10\%$ of the mass of the cold component ($\sim 2 \times 10^7 M_\odot$; Kamenetzky et al. 2012). Arp 220, on the other hand, is a nearby (77 Mpc; Scoville et al. 1997) ULIRG with an increased star formation rate that is the result of an ongoing merger in an advanced state. As in M82 and the

---

[13] Available from http://herschel.esac.esa.int/Docs/PACS/html/pacs_om.html.
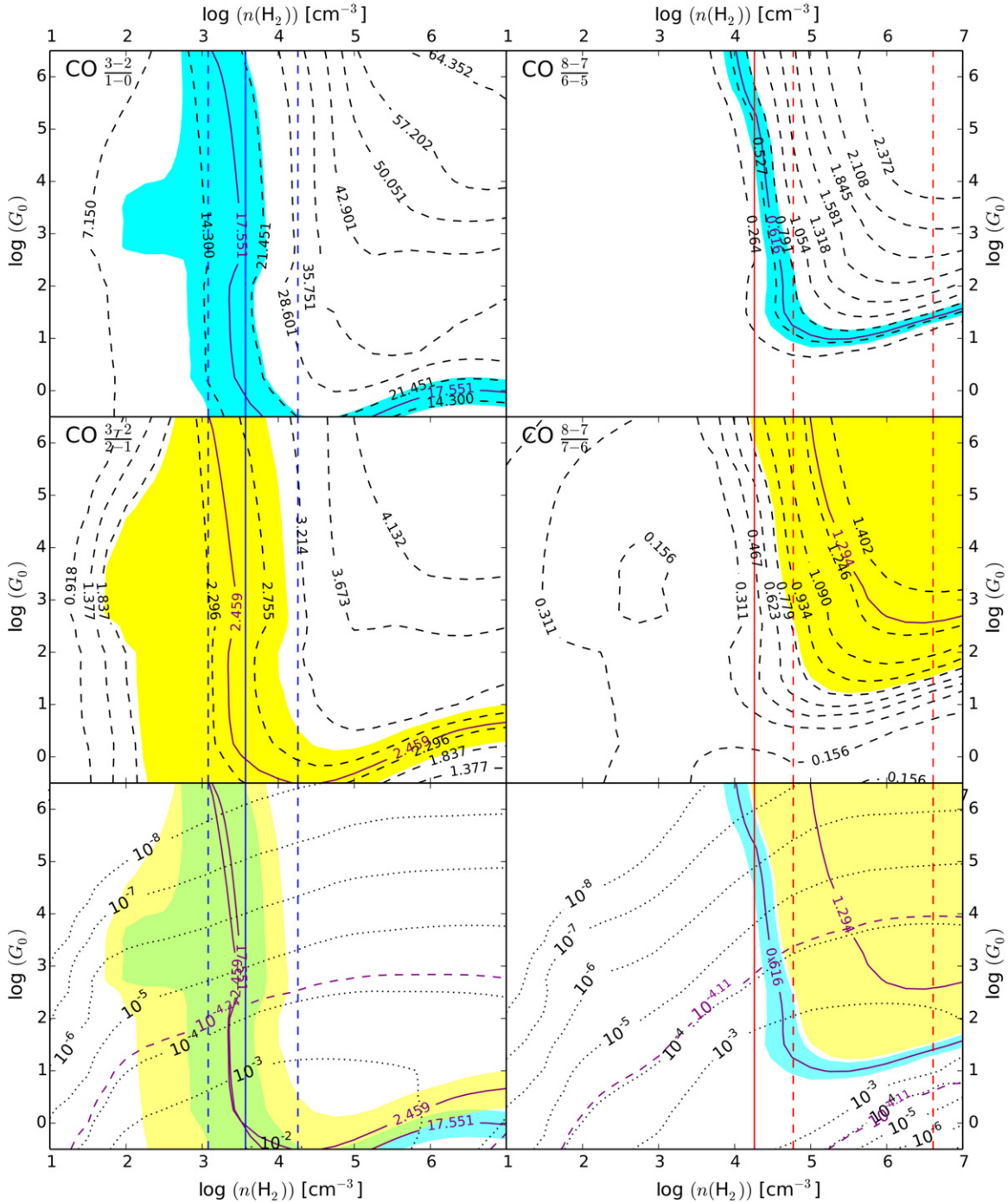[14] Available from http://www.astro.princeton.edu/~ganiano/Kernels.html.

Figure 13. PDR models for NGC 4038 comparing CO line ratios with the field strength in units of the Habing field (G_0) and the gas density (n_{H_2}). Each of the panels in the top two rows corresponds to a different CO ratio: $J = 3–2/1–0$ (top left), $J = 3–2/2–1$ (middle left), $J = 8–7/6–5$ (top right), and $J = 8–7/7–6$ (middle right). The $J = 3–2/1–0$ and $J = 3–2/2–1$ ratios are combined in the bottom left panel, while the $J = 8–7/6–5$ and $J = 8–7/7–6$ ratios are combined in the bottom right panel. The dashed black contours correspond to contours of constant ratios, while the purple contour corresponds to the measured ratio of the two lines. The blue and yellow shaded regions indicate the 1σ uncertainty range in the measured ratio. The blue and red solid lines correspond to the cold and warm component densities, as determined from the $J_{break} = 4$ radiative transfer solution for both CO and [C I], while the blue and red dashed lines correspond to the 1σ range to this density for the cold and warm components, respectively. In the bottom panels, the dashed purple contours corresponds to the measured ratio of CO $J = 3–2/FIR$ (bottom left) and CO $J = 6–5/FIR$ (bottom right) in units of erg cm^{-2} s^{-1} sr^{-1}, while the dotted black contours correspond to the model CO/FIR values.

(A color version of this figure is available in the online journal.)

Antennae, both a cold ($T_{kin} \sim 50$ K) and a warm (~ 1300 K) components are recovered from the radiative transfer analysis, albeit significantly warmer in Arp 220 (Rangwala et al. 2011). Similarly to M82, the warm gas mass ($\sim 4.7 \times 10^8\ M_\odot$) is about $\sim 10\%$ that of the cold gas mass ($\sim 5.2 \times 10^9\ M_\odot$; Rangwala et al. 2011).

Both Arp 220 and M82 have a significantly higher warm gas mass fraction than in the Antennae, where we found a warm gas mass fraction of $\sim 0.2\%$. This may be due to either Arp 220 and M82 having a larger source of heating or NGC 4038/39 cooling more efficiently. Evidence suggests that Arp 220 hosts a central AGN (Clements et al. 2002; Iwasawa et al. 2005);
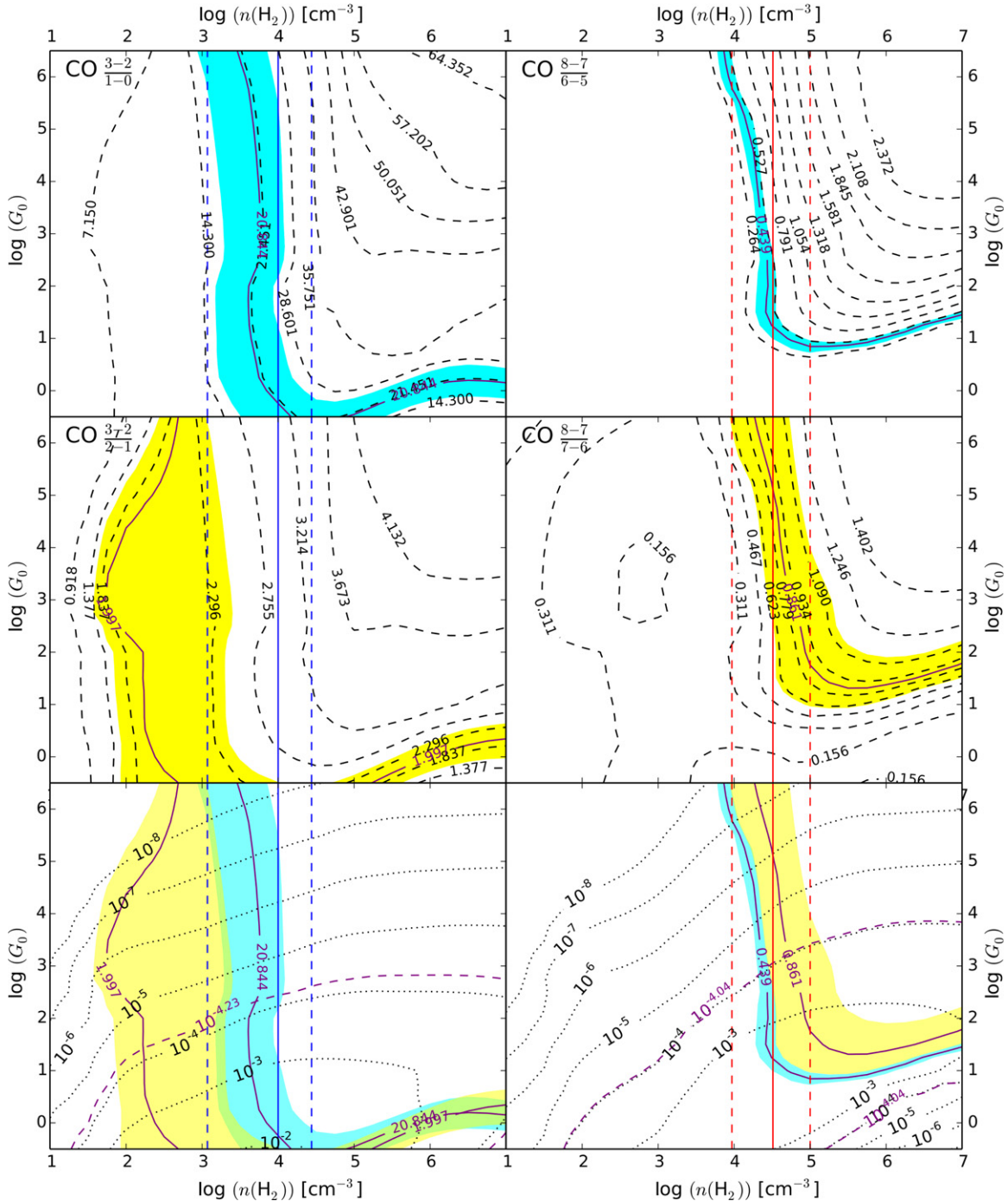
Figure 14. Same as Figure 13, except for NGC 4039.
(A color version of this figure is available in the online journal.)

however, the strongest candidates for heating are supernova and stellar winds, which contribute $\sim 200\, L_\odot/M_\odot$ to the overall heating (Rangwala et al. 2011). (This value does not account for supernova feedback efficiency.) The majority of the cooling is from H_2 due to the high temperature of the warm molecular gas ($T_{kin} \sim 1300$ K) and the cooling rate is $\sim 20\, L_\odot/M_\odot$. In Arp 220, a supernova heating efficiency $\gtrsim 0.1$ is required to match the cooling; however, Arp 220 is compact in comparison with the Antennae with the size of its molecular region only ~ 400 pc. Therefore, the increase in both the temperature and mass fraction of the warm molecular gas in Arp 220 is likely a result of a larger amount of supernova and stellar wind energy

being injected into the surrounding ISM, a higher supernova feedback efficiency, and a larger difference between the heating and cooling rates.

Similarly to Arp 220, turbulent motions due to supernovae and stellar winds are the strongest candidate for molecular gas heating in M82 (Panuzzo et al. 2010; Kamenetzky et al. 2012). The cooling rate in M82 is greater than in NGC 4038/39 by two orders of magnitude (3 $L_\odot/M_\odot$). The supernova rate in M82 is ~ 0.09 yr^{-1} (Fenech et al. 2010), which corresponds to $L_{SN} \sim (7 \times 10^8)\, L_\odot$ or $L_{SN}/M \sim 32\, L_\odot/M_\odot$ assuming a molecular gas mass of $2.2 \times 10^7\, M_\odot$ (Kamenetzky et al. 2012). A supernova feedback efficiency of ~ 0.1 is required
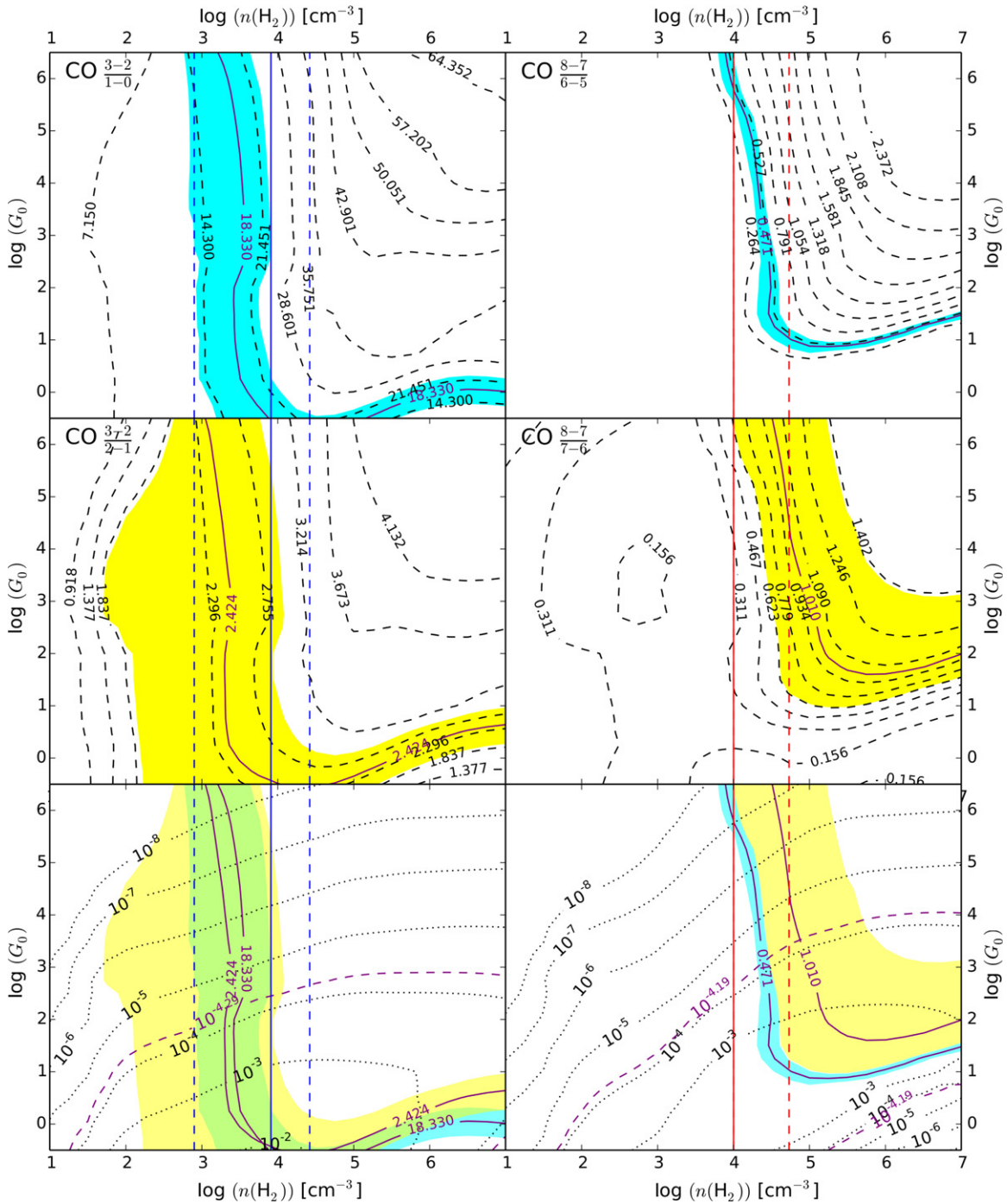
Figure 15. Same as Figure 13, except for the overlap region. Note that in the right column, the solid red line overlaps with the lower dashed red line.
(A color version of this figure is available in the online journal.)

to match the cooling in M82. As such, the higher warm gas fraction and temperature in M82 is possibly the result of a higher supernova heating rate, likely in part due to the increased supernova feedback efficiency.

5. SUMMARY AND CONCLUSIONS

In this paper, we present maps of the CO $J = 4$–3 to $J = 8$–7 and two [C I] transitions of the Antennae observed using the *Herschel* SPIRE-FTS. We supplement the SPIRE-FTS maps with observations of CO $J = 2$–1 and $J = 3$–2 from the JCMT,

CO $J = 1$–0 from the NRO, and observations of [C II] and [O I] 63 μm from the *Herschel* PACS spectrometer.

1. We perform an LTE analysis using the two observed [C I] transitions across the entire galaxy. We find that throughout the Antennae there is cold molecular gas with temperatures ~10–30 K. Our non-LTE radiative transfer analysis using both CO and [C I] transitions shows that the [C I] emission is optically thin, which suggests that [C I] is in LTE.

2. Using the non-LTE radiative transfer code RADEX, we perform a likelihood analysis using our eight CO transitions, both with and without the two [C I] transitions.

We find that the molecular gas in the Antennae is in both a cold ($T_{kin} \sim$ 10–30 K) and a warm ($T_{kin} \gtrsim$ 100 K) state, with the warm molecular gas comprising only $\sim$0.2% of the total molecular gas fraction in the Antennae. Furthermore, the physical state of the molecular gas does not vary substantially, with the pressure of both the warm and cold components being nearly constant within uncertainties and our angular resolution across the Antennae.

3. By considering the contributions of H_2, [C II], [O I] 63 μm, and CO, we calculate a total cooling rate of $\sim$2.0 × 10^8 $L_\odot$ for the molecular gas or $\sim$0.01 $L_\odot/M_\odot$, with [C II] as the dominant coolant. The contributions calculated for H_2 and [O I] 63 μm are lower limits due to unconstrained temperatures from the radiative transfer analysis (H_2) and limits on the size of the map ([O I] 63 μm). Furthermore, the contributions from [C II] are upper limits as some of the [C II] emission likely originates from atomic gas. Mechanical heating is sufficient to match the total cooling and heat the molecular gas throughout the Antennae, with both turbulent heating due to the ongoing merger and supernovae and stellar winds contributing to the mechanical heating.

4. We model the ratio of the CO flux to the FIR flux for CO $J = 3$–2 and $J = 6$–5, along with the ratio of various CO lines in the nucleus of NGC 4038, the nucleus of NGC 4039, and the overlap region using models of PDRs. Using the densities calculated from our non-LTE radiative transfer analysis, we find that a PDR with a field strength of $G_0 \sim 1000$ can explain the warm-component CO and FIR emission in all three regions. We also find that this field strength is consistent with the observed peak FIR flux in all three regions. These results are consistent with a previous study by Schulz et al. (2007). While PDRs are not necessary to heat the molecular gas, they remain as a possible contributor in heating the molecular gas in the star-forming regions of the Antennae.

5. Both the warm gas fraction and temperature are smaller in NGC 4038/39 than in either Arp 220 or M82, both of which are likely heated by turbulent motion due to supernova and stellar winds. We suggest that this is due to increased supernova feedback efficiency in both Arp 220 and M82 due to their compactness.

6. In the warm molecular gas, we calculate a CO abundance of $x_{CO} \sim 3 \times 10^{-5}$, corresponding to a warm molecular gas mass of $\sim$2.2 × 10^7 $M_\odot$. If we assume the same CO abundance in the cold molecular gas, this corresponds to a cold molecular gas mass of 1.5×10^{10} $M_\odot$ and a CO luminosity-to-mass conversion factor of $\alpha_{CO} \sim 7$ $M_\odot$ pc^{-2} (K km s^{-1})$^{-1}$, comparable to the Milky Way value. This value is consistent with previous results for the Antennae (Wilson et al. 2003), where the luminosity-to-mass conversion factor was determined using the virial mass of resolved SGMCs.

REFERENCES

Aniano, G., Draine, B. T., Gordon, K. D., & Sandstrom, K. 2011, PASP, 123, 1218
Bayet, E., Gerin, M., Phillips, T. G., & Contursi, A. 2006, A&A, 460, 467
Bendo, G. J., Boselli, A., Dariush, A., et al. 2012, MNRAS, 419, 1833
Bradford, C. M., Stacey, G. J., Nikola, T., et al. 2005, ApJ, 623, 866
Brandl, B. R., Snijders, L., den Brok, M., et al. 2009, ApJ, 699, 1982
Clements, D. L., McDowell, J. C., Shaked, S., et al. 2002, ApJ, 581, 974
Clements, D. L., Sutherland, W. J., McMahon, R. G., & Saunders, W. 1996, MNRAS, 279, 477
Cluver, M. E., Jarrett, T. H., Kraan-Korteweg, R. C., et al. 2010, ApJ, 725, 1550
Currie, M. J., Draper, P. W., Berry, D. S., et al. 2008, in ASP Conf. Ser. 394, Astronomical Data Analysis Software and Systems XVII, ed. R. W. Argyle, P. S. Bunclark, & J. R. Lewis (San Francisco, CA: ASP), 650
Dale, D. A., & Helou, G. 2002, ApJ, 576, 159
Dale, D. A., Helou, G., Contursi, A., Silbermann, N. A., & Kolhatkar, S. 2001, ApJ, 549, 215
Downes, D., & Solomon, P. M. 1998, ApJ, 507, 615
Fenech, D., Beswick, R., Muxlow, T. W. B., Pedlar, A., & Argo, M. K. 2010, MNRAS, 408, 607
Fischer, J., Shier, L. M., Luhman, M. L., et al. 1996, A&A, 315, L97
Fulton, T. R., Baluteau, J., Bendo, G., et al. 2010, Proc. SPIE, 7731, 773134
Gao, Y., Lo, K. Y., Lee, S.-W., & Lee, T.-H. 2001, ApJ, 548, 172
Gehrz, R. D., Sramek, R. A., & Weedman, D. W. 1983, ApJ, 267, 551
Genzel, R., Tacconi, L. J., Gracia-Carpio, J., et al. 2010, MNRAS, 407, 2091
Griffin, M. J., Abergel, A., Abreu, A., et al. 2010, A&A, 518, L3
Herrera, C. N., Boulanger, F., Nesvadba, N. P. H., & Falgarone, E. 2012, A&A, 538, L9
Hibbard, J. E. 1997, in AIP Conf. Ser. 393, The Seventh Astrophysical Conference: Star Formation, Near and Far, ed. S. S. Holt & L. G. Mundy (Melville, NY: AIP), 259
Hollenbach, D., Kaufman, M. J., Neufeld, D., Wolfire, M., & Goicoechea, J. R. 2012, ApJ, 754, 105
Hunter, J. D. 2007, CSE, 9, 90
Ikeda, M., Oka, T., Tatematsu, K., Sekimoto, Y., & Yamamoto, S. 2002, ApJS, 139, 467
Iwasawa, K., Sanders, D. B., Evans, A. S., et al. 2005, MNRAS, 357, 565
Joseph, R. D., & Wright, G. S. 1985, MNRAS, 214, 87
Kamenetzky, J., Glenn, J., Maloney, P. R., et al. 2011, ApJ, 731, 83
Kamenetzky, J., Glenn, J., Rangwala, N., et al. 2012, ApJ, 753, 70
Klaas, U., Nielbock, M., Haas, M., Krause, O., & Schreiber, J. 2010, A&A, 518, L44
Le Bourlot, J., Pineau des Forêts, G., & Flower, D. R. 1999, MNRAS, 305, 802

Leroy, A. K., Bolatto, A., Gordon, K., et al. 2011, ApJ, 737, 12
Malhotra, S., Kaufman, M. J., Hollenbach, D., et al. 2001, ApJ, 561, 766
Maloney, P. R. 1999, Ap&SS, 266, 207
Mao, R. Q., Henkel, C., Schulz, A., et al. 2000, A&A, 358, 433
Meijerink, R., Kristensen, L. E., Weiß, A., et al. 2013, ApJL, 762, L16
Naylor, B. J., Bradford, C. M., Aguirre, J. E., et al. 2010a, ApJ, 722, 668
Naylor, D. A., Baluteau, J.-P., Barlow, M. J., et al. 2010b, Proc. SPIE, 7731, 773116
Neff, S. G., & Ulvestad, J. S. 2000, AJ, 120, 670
Nikola, T., Genzel, R., Herrmann, F., et al. 1998, ApJ, 504, 749
Oberst, T. E., Parshley, S. C., Stacey, G. J., et al. 2006, ApJL, 652, L125
Panuzzo, P., Rangwala, N., Rykala, A., et al. 2010, A&A, 518, L37
Papadopoulos, P. P., Thi, W.-F., & Viti, S. 2004, MNRAS, 351, 147
Papadopoulos, P. P., van der Werf, P., Xilouris, E., Isaak, K. G., & Gao, Y. 2012, ApJ, 751, 10
Parkin, T. J., Wilson, C. D., Foyle, K., et al. 2012, MNRAS, 422, 2291
Pereira-Santaella, M., Spinoglio, L., Busquet, G., et al. 2013, ApJ, 768, 55
Pilbratt, G. L., Riedinger, J. R., Passvogel, T., et al. 2010, A&A, 518, L1
Rangwala, N., Maloney, P. R., Glenn, J., et al. 2011, ApJ, 743, 94
Read, A. M., Ponman, T. J., & Wolstencroft, R. D. 1995, MNRAS, 277, 397
Sanders, D. B., Mazzarella, J. M., Kim, D.-C., Surace, J. A., & Soifer, B. T. 2003, AJ, 126, 1607
Sanders, D. B., & Mirabel, I. F. 1996, ARA&A, 34, 749
Schöier, F. L., van der Tak, F. F. S., van Dishoeck, E. F., & Black, J. H. 2005, A&A, 432, 369
Schroder, K., Staemmler, V., Smith, M. D., Flower, D. R., & Jaquet, R. 1991, JPhB, 24, 2487
Schulz, A., Henkel, C., Muders, D., et al. 2007, A&A, 466, 467

Schweizer, F., Burns, C. R., Madore, B. F., et al. 2008, AJ, 136, 1482
Scoville, N. Z., Yun, M. S., & Bryant, P. M. 1997, ApJ, 484, 702
Sliwa, K., Wilson, C. D., Petitpas, G. R., et al. 2012, ApJ, 753, 46
Spinoglio, L., Pereira-Santaella, M., Busquet, G., et al. 2012, ApJ, 758, 108
Stanford, S. A., Sargent, A. I., Sanders, D. B., & Scoville, N. Z. 1990, ApJ, 349, 492
Swinyard, B. M., Ade, P., Baluteau, J.-P., et al. 2010, A&A, 518, L4
Thornton, K., Gaudlitz, M., Janka, H.-T., & Steinmetz, M. 1998, ApJ, 500, 95
Tielens, A. G. G. M., & Hollenbach, D. 1985, ApJ, 291, 722
Toomre, A., & Toomre, J. 1972, ApJ, 178, 623
Ueda, J., Iono, D., Petitpas, G., et al. 2012, ApJ, 745, 65
van der Tak, F. F. S., Black, J. H., Schöier, F. L., Jansen, D. J., & van Dishoeck, E. F. 2007, A&A, 468, 627
van der Werf, P. P., Isaak, K. G., Meijerink, R., et al. 2010, A&A, 518, L42
Ward, J. S., Zmuidzinas, J., Harris, A. I., & Isaak, K. G. 2003, ApJ, 587, 171
Warren, B. E., Wilson, C. D., Israel, F. P., et al. 2010, ApJ, 714, 571
Wei, L. H., Keto, E., & Ho, L. C. 2012, ApJ, 750, 136
Whitmore, B. C., Chandar, R., Schweizer, F., et al. 2010, AJ, 140, 75
Whitmore, B. C., & Schweizer, F. 1995, AJ, 109, 960
Whitmore, B. C., Zhang, Q., Leitherer, C., et al. 1999, AJ, 118, 1551
Wilson, C. D., Scoville, N., Madden, S. C., & Charmandaris, V. 2000, ApJ, 542, 120
Wilson, C. D., Scoville, N., Madden, S. C., & Charmandaris, V. 2003, ApJ, 599, 1049
Wolfire, M. G., Hollenbach, D., & McKee, C. F. 2010, ApJ, 716, 1191
Yun, M. S., Ho, P. T. P., & Lo, K. Y. 1993, ApJL, 411, L17
Zhang, H.-X., Gao, Y., & Kong, X. 2010, MNRAS, 401, 1839
Zhu, M., Seaquist, E. R., & Kuno, N. 2003, ApJ, 588, 243